MPI–PhE/98–3

THE
FORWARD TIME PROJECTION CHAMBER
FOR THE STAR DETECTOR
PROPOSAL

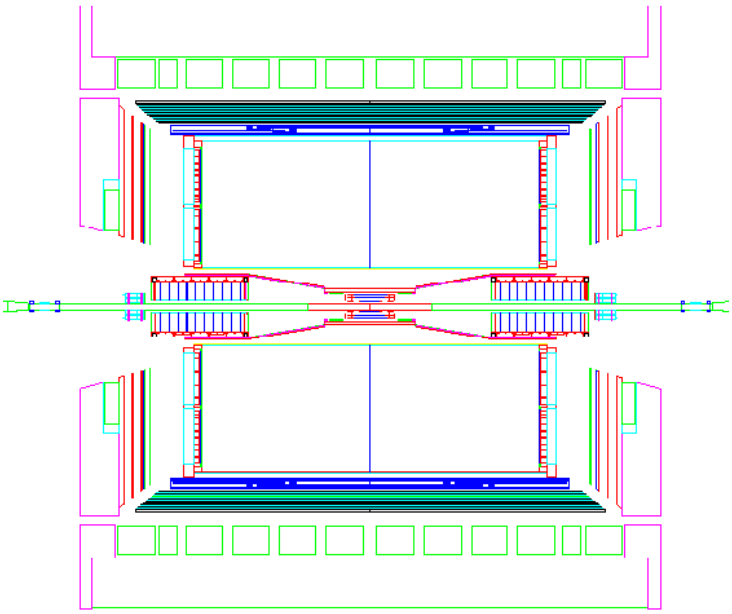

THE STAR FTPC COLLABORATION

30 January 1998

The STAR FTPC Collaboration

Lawrence Berkeley National Laboratory

F. Bieser, S. Klein, H.-G. Ritter, H. Wieman
LBNL, Berkeley, CA 94720, USA

Brookhaven National Laboratory

A. Etkin, K. Foley, T. Hallmann, M. LeVine, R. Longacre, B. Love, A. Saulys
BNL, Physics Dept., Upton, NY 11973-5000, USA

University of California at Davis

M. Anderson, P. Brady, B. Caskey, D. Cebra, J. Draper, M. Heffner, J. Klay, J. Romero, L. Wood
UC Davis, Dept. of Physics, Davis, CA 95616, USA

University of California at Los Angeles

V. Ghazikhanian
UCLA, Physics Dept., Los Angeles, CA 90095-1547, USA

Max-Planck-Institut für Physik

X. Bittl, V. Eckardt, H. Fessler, W. Gong, H. Hümmler, M. Konrad, R. Marstaller, E. Schäfer, N. Schmitz, A. Schüttauf, P. Seyboth, J. Seyboth
Max-Planck-Institut für Physik, 80805 München, Germany

Moscow Engineering Physics Institute

A. Lebedev
MEPhI, Moscow 115409, Russia

Contents

1 Introduction

Nucleus-Nucleus collisions at RHIC are expected to produce baryon-rich matter near beam rapidity and nearly baryon-free matter at midrapidity. While the latter is mostly relevant for the study of the transition between hadronic matter and the quark gluon plasma (QGP), understanding the transfer of energy from beam rapidity to midrapidity is essential for understanding the space-time evolution of the collision. Energy transfer can be studied by following the fate of the baryons brought into the collision, in particular by measuring the net baryon number at intermediate rapidities.

Two forward time projection chambers (FTPCs) are proposed to nearly double the kinematic range covered by the STAR spectrometer. The central TPC tracks the pseudorapidity (η) range from -1.5 to $+1.5$ into which about 50% of the charged primary particles from central gold on gold events are emitted. The FTPCs increase the covered range by the interval $2.5 < |\eta| < 4.0$ with complete and uniform azimuthal (ϕ) coverage; an additional 30% of the charged particles are emitted into this range. The placement of the FTPCs inside the STAR solenoid (Fig. 1) allows for the determination of the charge of the particles as well as for the measurement of their momenta to an accuracy of about 12%. The FTPCs therefore give STAR an almost complete event characterisation.

The baryon number flow can be studied by measuring the difference in the distributions of positively charged and negatively charged ($N(+) - N(-)$) particles as a function of η. Selected event classes can then be investigated with regard to nuclear stopping. Because the matter radiating at midrapidity and intermediate rapidity are causally disconnected, the entropy densities (proportional to $dN/d\eta$) at midrapidity and intermediate rapidity can be compared in order to label events with unusually high entropy generation at midrapidity, corresponding possibly to a first order phase transition. The coverage of the central TPC extends over the η region where $dN/d\eta$ is approximately constant. The additional coverage provided by the FTPCs extends into the regions where the particle production is expected to be falling off rapidly as a function of increasing η. The coverage added by the FTPCs allows an accurate measurement of the width of the region of maximum $dN/d\eta$, allows an accurate determination of where the production fall-off occurs, and enhances the ability to resolve regions of anomalously high particle production. These regions of anomalously high particle production are expected to be associated with the decay of a QGP bubble. As the plasma is transformed into normal nuclear matter, large numbers of particles should be produced with small momenta in the rest frame of the bubble, i.e. in small regions of η space. These regions can be identified through analysis of the $dN/d\eta$ and the $dN/d\phi$ distributions particularly for low transverse momentum (p_t) particles.

Together with the photon multiplicity detector proposed by the Indian groups,

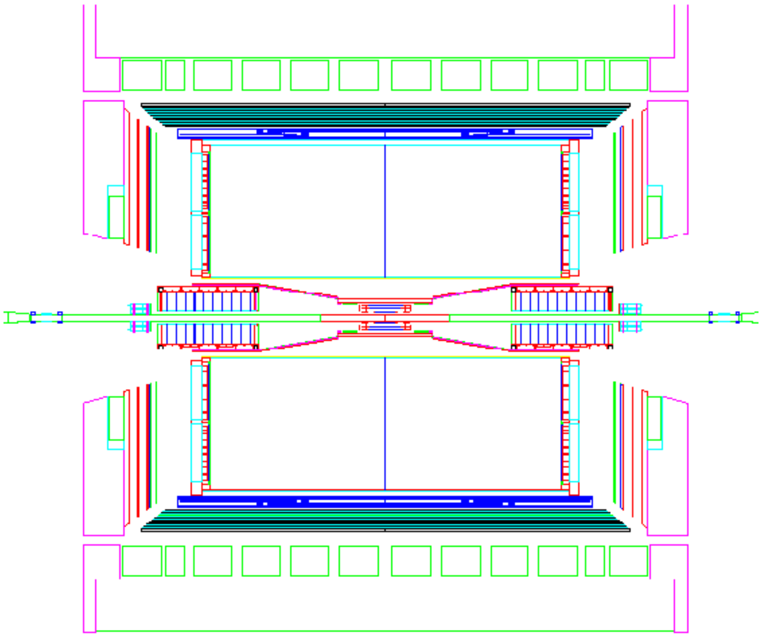

Figure 1: Cut view of the STAR detector showing the location of the FTPCs inside the STAR solenoid and the central TPC. The pseudo-rapidity range covered by the FTPCs is $2.5 < |\eta| < 4.0$

covering essentially the same η range as the FTPC's, a sensitive search for the disoriented chiral condensate (DCC) would be possible. If it were produced in large enough domains it would be detected by characteristic fluctuations of the ratio of charged particles to photons at low p_t.

The high-η regions are characterized by three technical challenges:

1. This region is generally characterized by a high spatial density of charged particles.

2. The charged-particle tracks tend to get more rigid at larger $|\eta|$, making curvature, time of flight, and relative dE/dx more difficult to measure.

3. A potentially large background of tracks from secondary interactions in the beampipe, requiring careful design in order to minimize material.

For these reasons, tracking in the forward region requires novel detector concepts, and careful scrutiny of these concepts has led to a series of refinements resulting in the current FTPC proposal.

In order to optimise the the phase-space acceptance and obtain high spatial and two-track resolution, a radial time projection chamber scheme is proposed for the FTPC's, where electrons drift in a radial electric field perpendicular to the axial solenoidal magnetic field. The FTPCs are located within the STAR solenoidal magnetic field (Fig. 1) in order to allow a measurement of the charge and momentum of the tracks. Fig. 2 shows a schematic view of the FTPC design. A curved wire chamber with pad readout will be used to register FTPC signals. The FTPC drift cathode, biased at a negative high-voltage, is a tube surrounding the beam pipe. The readout plates with their front-end electronics are mounted on an outer cylindrical frame. The drift and amplification regions are separated by two cylindrical grids of wires. One is the gating grid; the other serves as the ground grid. The drift field is defined by concentric rings of thin metal tubes on both entrance and exit planes. Voltages on the rings are defined by a resistor chain so that a radial $\boldsymbol{E}$ field is established.

The use of a high resolution wire chamber for TPC readout, as well as use of the proper gas, provide the good spatial resolution and two-track separation required for this position of the FTPC inside the solenoid where the track density is high. The reduced drift velocity of the chosen 'cool' gas is matched to the small radius of the FTPC. The cool gas has little diffusion of electrons, providing superior two-track resolution and position-measuring accuracy. Moreover, a small Lorentz angle gives only little bending of the drift path of the electrons perpendicular to the magnetic field.

The expected performance of the proposed FTPC design and the ability of the detector to achieve the physics goals for which it is intended are documented in the following sections.

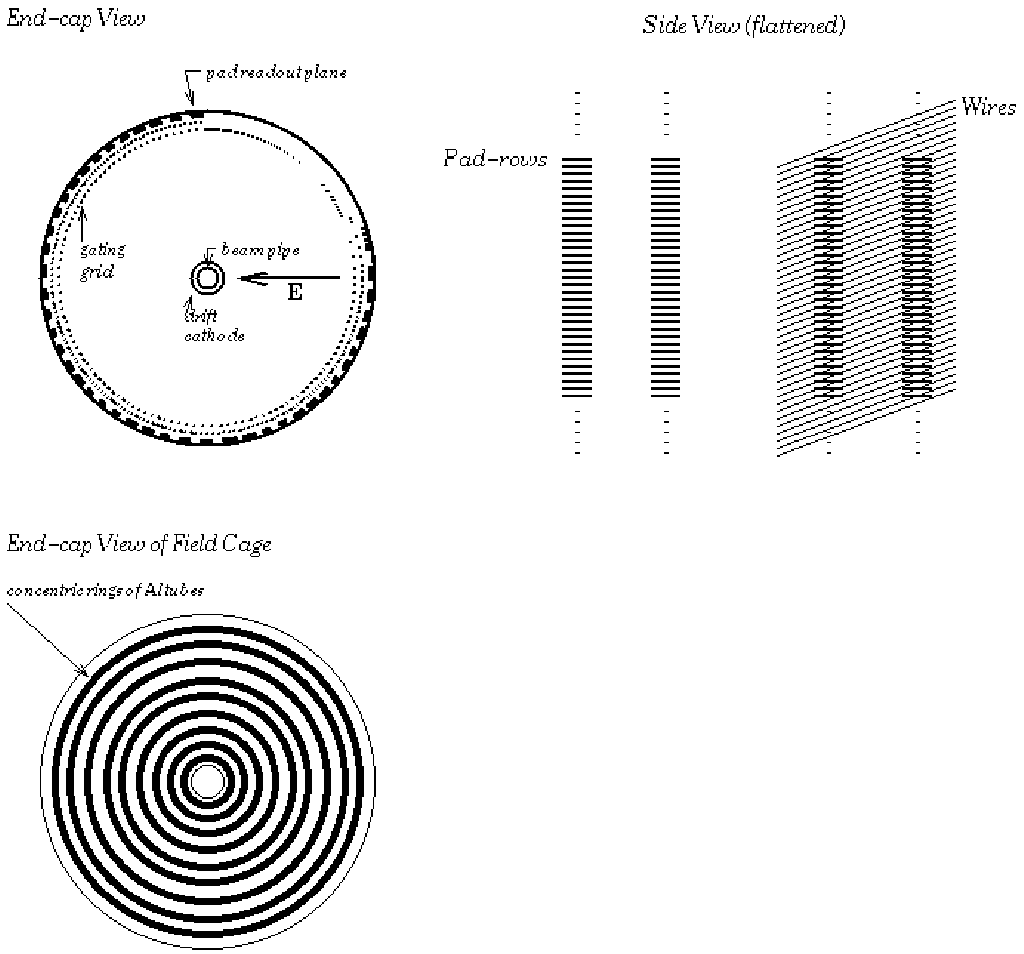

Figure 2: Radial TPC with pad readout.

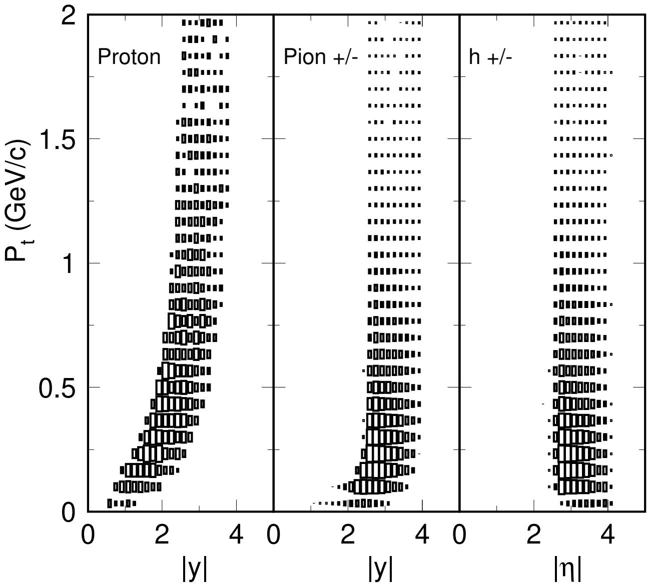

Figure 3: *p_t - y distributions of accepted protons (left) and charged pions (center) as well as p_t - η distribution for charged hadrons (right).*

2 Physics

2.1 Physics Summary

The FTPCs extend the tracking coverage of STAR in η space by nearly a factor of two, relative to the central TPC. Each FTPC covers approximately $2.5 < |\eta| < 4$ (Fig. 3). Of fundamentally greater importance, they extend the coverage into a qualitatively different region, in terms of physics. The midrapidity regime is expected to be the domain of a rather baryon-free plasma and of the hot hadronic gas that is left in the aftermath of its deflagration. The forward rapidity region ($|y| > 2$) is characterized by the strings and ropes in the fragmentation regime, and will contain the remnants of the original baryons of the projectile nuclei, modified by the rearrangement of the quark composition created in the collision. The shape of their distribution will provide a rather direct measure of the conversion of the energy of the colliding nuclei into thermal energy of the central region left by the receeding remnants of the projectile nucleons.

The approach that underlies the design of the STAR detector system has been to provide a comprehensive measurement of the charged particle flux on an event-by-event basis. The addition of the FTPC system complements the existing STAR subsystems, and allows an improvement of event-by-event global analysis, of individual event selection, and studies of additional physics subjects.

A traditional approach to understanding the underlying processes in relativistic heavy ion interactions is to compare the results of experiment with the predictions of models. In order for these comparisons to provide meaningful insight, it is necessary for the detector system to provide sufficient constraints to distinguish these various models. In order to achieve the largest 'resolving power', one should investigate phase space regions showing significant differences between these models, such as the forward regions. The various models that attempt to describe ultra-relativistic heavy-ion collisions give substantially different predictions for many observables. An example is the dN/dy spectrum of charged particles. In one model proposed by Geiger [gei95], for example, this observable is expected to exhibit a transition from the parton-cascade regime to the soft fragmentation regime. In this model it is found that the perturbative QCD parton production and cascade development provides an important contribution to particle production at central rapidities, and that the "afterburner" cascading of pre-hadronic clusters and formed hadrons emerging from the parton cascade is essential [gei97].

If this picture is correct, a modification of the dN/dy spectrum for charged particles and especially protons is expected within the acceptance of the FTPCs. Although the identification of protons by dE/dx in the FTPC is problematic, the proton rapidity distribution can be inferred through a $N(+) - N(-)$ analysis on an ensemble of several events. The charge resolution of the FTPCs is sufficient to accomplish this task on an event-by-event basis. However, the statistics of a small difference of large numbers in $N(+)$ and $N(-)$ do not allow for event-by-event analysis. It may also be possible that a detailed analysis of the differences of π^+ and π^- spectra at low p_t will elucidate the subtle differences, which are caused by the Coulomb forces of the proton remnants.

By exploiting the p_t spectra as a function of rapidity, one may study the temperature-parameter profile throughout the collision. The FTPCs allow for this on an event-by-event basis (see 2.2.1 below). This should provide some insight into the time evolution of the reaction. Moreover the shape of p_t spectra is expected to reflect the radial component of flow.

A subject of considerable interest in the framework of QGP signatures is 'disoriented chiral condensates' (DCC) [raj93]. They have recently been proposed as potential signatures of chiral symmetry restoration. Much of the theory about DCCs is based on the linear sigma model. In a plasma where all masses vanish, the energy does not depend on the orientation of the chiral field in $\pi - \sigma$ space. When it cools to normal matter with finite-mass pions the chiral field direction may not coincide with the true-vacuum direction in some domains. Assuming that the disoriented angle, about which the field is oscillating, is equally probable anywhere in the space (π_3, π_2, π_1) of meson-type orientations, then the probability of ratios of the number of neutral pions to all pions can be estimated [raj93]. Denoting this ratio by R, the relative probability of R is found to be $0.5/\sqrt{R}$. This means that the probability for $R < 0.01$ is 10%, or $R < 0.05$ is 22%! This contrasts to the measured value $R = 1/3$ from typical hadronic collisions, resulting from a binomial distribution.

Whereas the theory is uncertain about size and energy density of these domains, it has been proposed that they may cool rapidly ("quenched"). This may result in DCC domains of size and local energy density sufficiently large for experimental detection. Inasmuch as the FTPCs are in a region of smaller $dN/d\eta$ than at midrapidity, these DCCs may stand out from standard processes, and may thus be detectable. The numbers of negative and of positive pions should be essentially equal. Depending on the orientation of the chiral field, there may be an enhancement of neutral pions, relative to charged pions. The ideal situation would be to detect an unusually large (small) number of charged pions in an FTPC together with an exceptionally small (large) number of neutral pions in the same phase space region. The neutral pions could be detected via their decay photons in a photon multiplicity detector behind the FTPCs. This measurement could in prinicple be done on an event-by-event basis, placing a limit on the size of DCC domains that might be formed.

Given the energy densities possible in the hadronization of quark matter droplets, it is another interesting possibility that more than one boson occupies a quantum cell, in which case Bose-Einstein enhancement of charged pion production may occur. This is sometimes called pion laser action [pra93]. The relative momenta of these charged pions are quite small, i.e. about 100 MeV/c. Given the azimuthal coverage and momentum resolution of the proposed FTPC design, detection of the phenomenon should be possible.

Note that the capability for this measurement depends strongly on the FTPCs' excellent granularity in η and ϕ and their good momentum resolution, which gives efficient background rejection; all this is a consequence of the FTPCs being real tracking devices and not just a single plane of pixel detectors. Furthermore, the low-momentum charged pions of the hypothetical DCC would be differentially spread in space because of the magnetic field, even if they left the interaction point at the same angle, but with different momenta. The tracking of the FTPCs can retrace them back to give their momentum vectors, close to what they were when they left the interaction point. To achive optimal performance, it is also necessary to reduce background as much as possible, i.e. a low-Z beam pipe is required.

To illustrate the need for FTPCs in the STAR experiment, pseudorapidity distributions from individual events obtained from 5 event generators [lon] are displayed in Figs. 4 to 6. These event generators have recently been used by the level-1 trigger group [mil95] for detailed trigger studies.

The basic generator is an optimized version of HIJET which considers, e.g., Au+Au collisions as a sum of independent nucleon-nucleon interactions. The generator PLASMA is derived from HIJET by assigning energy and momentum of

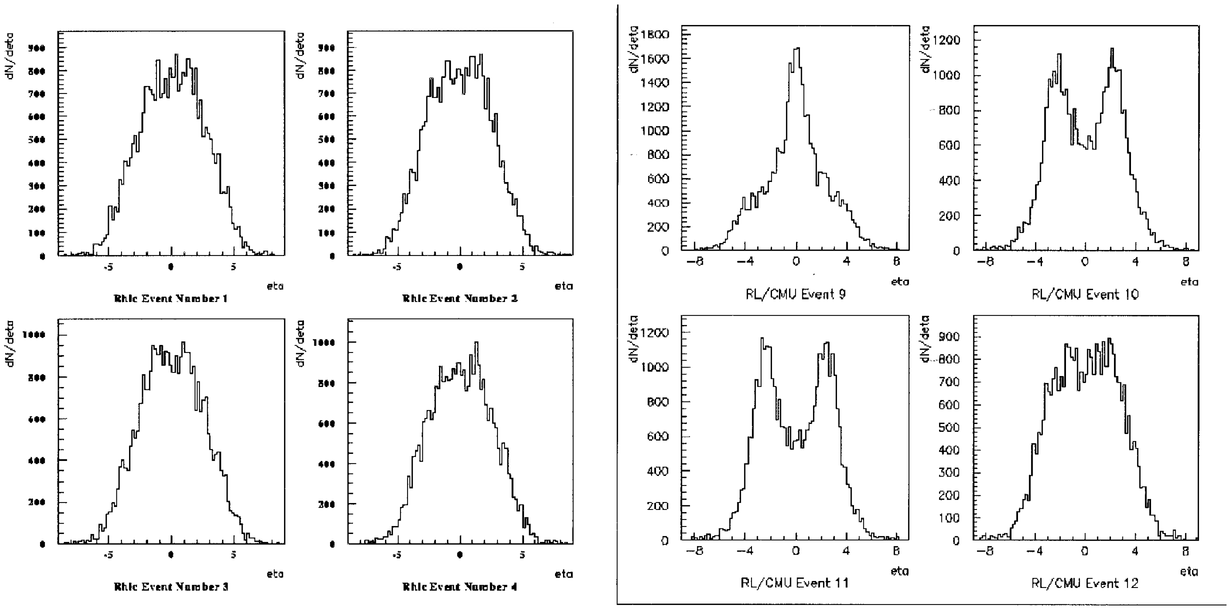

Figure 4: Psuedo-rapidity density $dN/d\eta$ for charged particles; on the left are four random events; on the right are four selected PLASMA events.

particles from a certain volume in the Au-Au overlap region to spherically expanding bubbles in the QGP phase; these bubbles hadronize subsequently in a consistent fashion and yield local maxima in the rapidity distributions with a typical width $\sigma_y \approx 1$. The generator CHIRAL transforms the QGP bubbles of PLASMA into a pion gas at a temperature of 70 MeV and with a charge ratio R following a probability distribution $P(R) \propto 1/\sqrt{R}$, as above. The code LANDAU adds longitudinal expansion to the bubbles of PLASMA. Finally, the generator SMOKE deforms the QGP bubbles of PLASMA into 'pancakes' such that final state hadrons emerge at nearly identical polar angles, thus resembling smoke rings.

Summarizing Figs. 4 to 6 of $dN/d\eta$, the substantially varying structures are only partially explored by the central TPC (tracking to about $|\eta| = 1.5$), while the addition of the FTPCs is vital for recognizing differences between such phenomena. Additionally, the ability of the FTPCs to measure momentum to 10-15 % and charge sign with high reliability, as well as accurate measurements of η and ϕ, are crucial for extracting the physics of unusual event structures, event-by-event.

The importance and uniqueness of the FTPCs is further illustrated for asymmetric collisions or peripheral interaction triggers. In both cases there is substantial particle flux away from the midrapidity region for which the baseline STAR detection capabilities are optimized. In order to understand the bulk-property nature of heavy-ion collisions, it will be necessary to explore p+A collisions. The latter contain multiple interactions of the incident particles and of their daughters as they

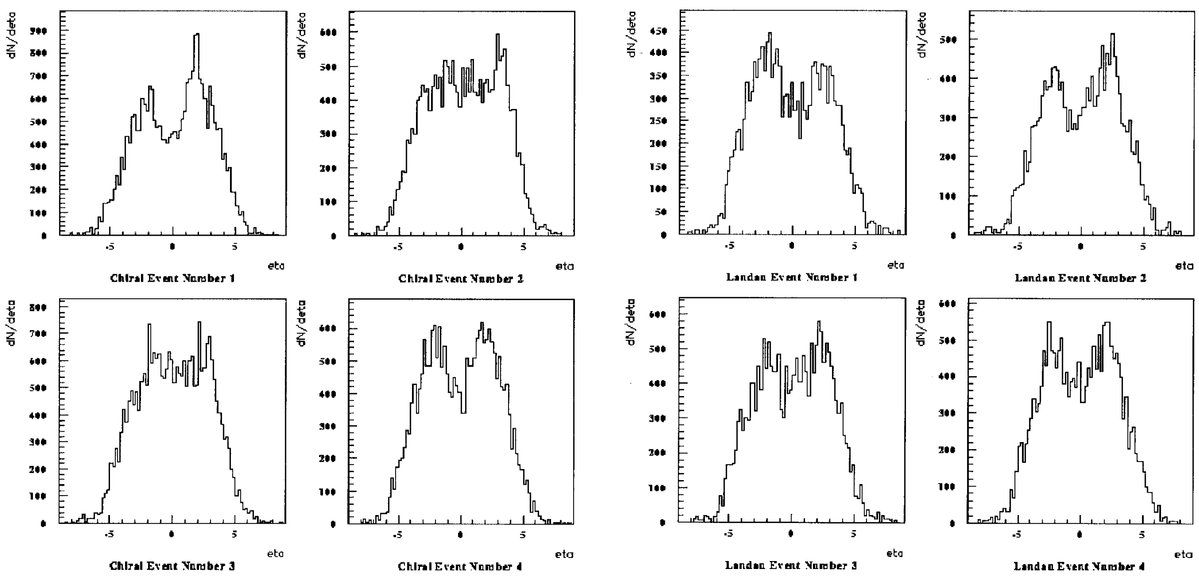

Figure 5: Pseudo-rapidity density $dN/d\eta$ for charged particles; on the left are four CHIRAL events; on the right are four LANDAU events.

cascade through the nucleus. This multiple interaction process is not expected to result in plasma formation. It can, however, produce signals that obfuscate the identification of plasma formation in A+A collisions. Therefore, asymmetric beams will be an important part of the basic STAR physics program. In asymmetric collisions, the production of particles will dominate in one of the two forward cones. For p+Au interactions we will show below (2.2.1) that much of the region of interest is then outside the acceptance of the central TPC, but is covered by the FTPCs.

STAR also hopes to measure the shadowing of the gluon structure function in the Au nucleus directly to remove this kind of uncertainty in the interpretation of spectra measured in Au+Au interactions. This involves studying gamma + jet final states in p+Au interactions. The additional tracking acceptance of the FTPCs will be very important in reconstructing the jet properly.

Another aspect of the STAR scientific program, for which the FTPC detection capability is essential, is the study of highly peripheral interactions which explore a very different physics regime. Due to the large charges, the colliding Au nuclei will emit very intense virtual photon fields. These are the origin of photon-photon collisions in Au+Au collisions at very large impact parameters where there are no strong interactions. The resulting final state includes only a few charged particles, measured in the central TPC. Background is efficiently reduced when the FTPCs detect no particles from this event. Also possible is a double-pomeron intermediate state. These are considered to be glue-rich, and are thus a fertile hunting ground for

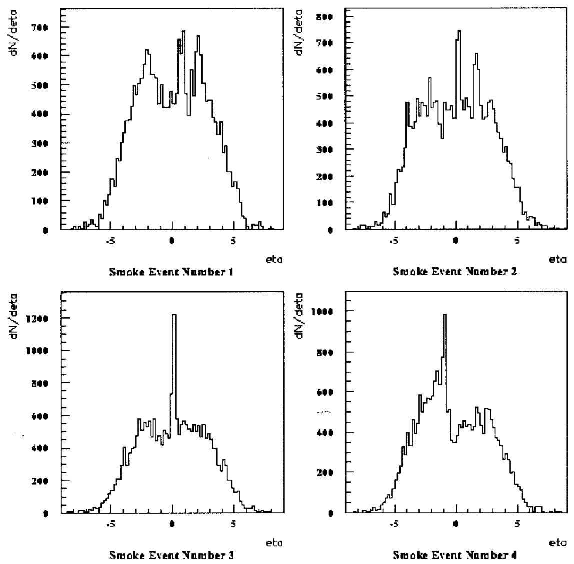

Figure 6: Pseudo-rapidity density $dN/d\eta$ for charged particles; four SMOKE events.

glueballs. Photon-photon processes are believed to disfavor glueballs, but to couple favorably to four-quark states.

The production of strange particles is expected to be valuable for analysing bulk-matter effects. The SVT, TPC, and TOF systems all list strange-particle production as a key physics program. A study of V^0s in the FTPCs could complement these results and enrich the STAR physics program. Feasibility studies are underway, the decay vertex identification being difficult.

2.2 Physics Simulations

2.2.1 Central Collisions

We have compared the predictions of the standard HIJING model [wan91] to those of a modified chiral model [lon] and to Geiger's parton cascade model, VNI [gei97]. These models incorporate quite different assumptions as to the nature of the underlying physics processes. The HIJING model assumes a soft picture for the fundamental interactions, i.e. string formation between pairs of interacting partons, stretching of the strings, and later breakup into hadrons. VNI assumes hard and semi-hard processes where partons are formed immediately and are later clustered to form hadrons. The CHIRAL model shown here was developed by Longacre [lon]. It uses the HIJET model, removes energy from the outgoing particle flux and rechannels that energy into localized clusters of pions to simulate the expected signature of the decay of a disoriented chiral condensate.

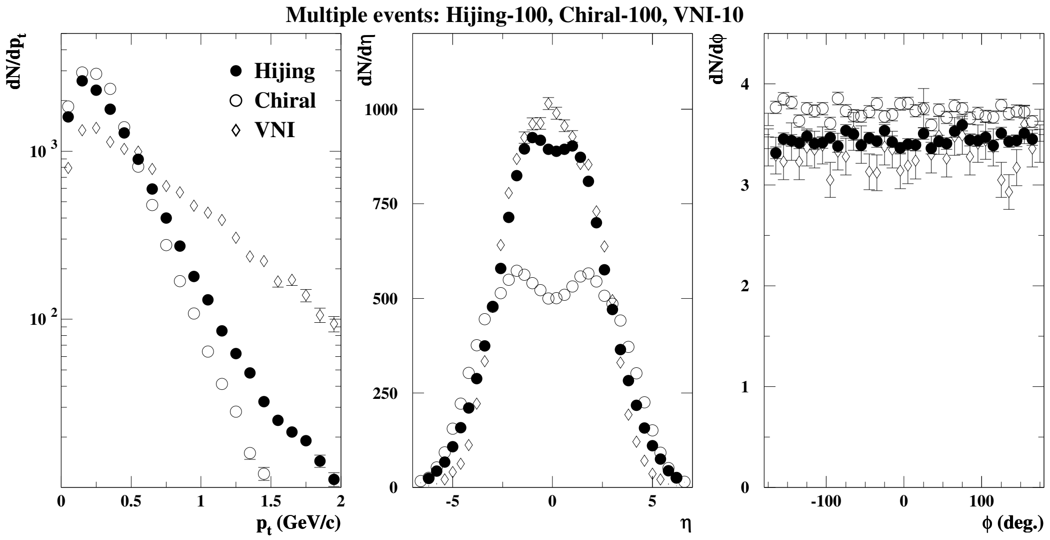

Figure 7: Distributions of charged particles normalised per event: $\frac{dN}{dp_T}$ (left), $\frac{dN}{d\eta}$ (middle), and $\frac{dN}{d\phi}$ (right) using multiple events. Three event generators are used: ($\bullet$) HIJING (100 events), ($\circ$) CHIRAL (100 events), and ($\diamond$) VNI (10 events). The spectra $\frac{dN}{dp_T}$, $\frac{dN}{d\phi}$ are for $\mid \eta \mid= 2.5$ - 4.0.

Figure 7 shows the results for an ensemble of events from each model. In the middle panel is $dN/d\eta$ for charged particles. The left- and right-hand panels display dN/dp_T and $dN/d\phi$, respectively, for particles emitted into the η acceptance of the FTPCs. In the left-hand panel, dN/dp_T shows clear differences for the three models. The parton cascade produces a much higher temperature parameter than HIJING. The HIJING model and CHIRAL model, which is based on HIJET, show a similar temperature parameter. However, one sees a transfer of particles (mostly pions) from the high-p_T region to the low-p_T region. For the ensemble of 100 events in the right-hand panel, one would expect no significant dependence on azimuthal angle, regardless of the model, and there is none within statistical uncertainty.

Similar plots are shown in Fig. 8 for a single event from each of these models. It is apparent from the left-hand panel that the temperature parameter can be obtained event-by-event with good accuracy. This can be illustrated by comparing the generated and reconstructed p_T spectrum of a single HIJING event as shown in Fig. 9. The agreement in both rapidity intervals is excellent. The low-p_T enhancement of the CHIRAL model can also be detected in a single event, as tracking is satisfactory down to $p_T \approx 70$ MeV/c. For this single event there is the possibility for a DCC to

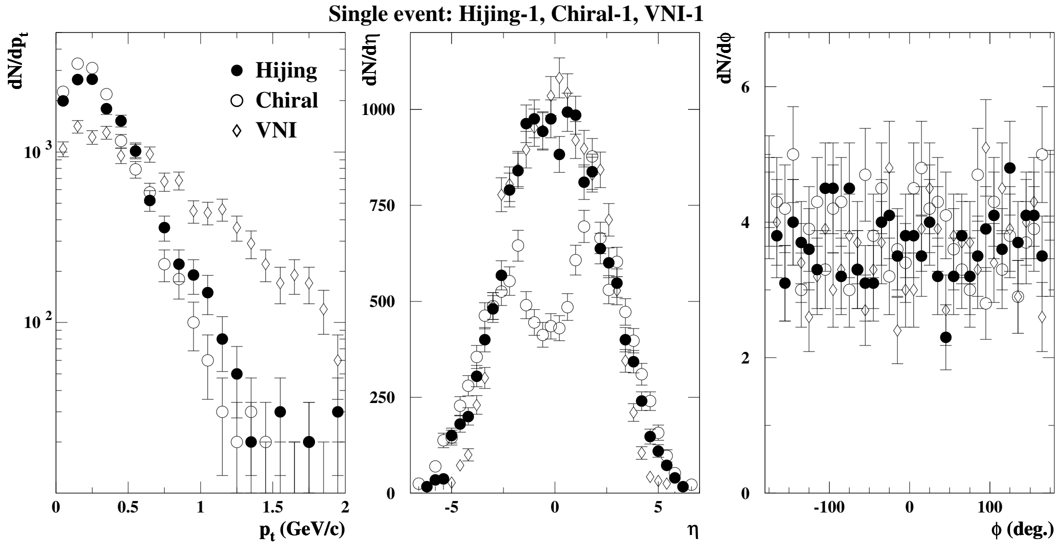

Figure 8: Distributions of charged particles: $\frac{dN}{dp_T}$ (left), $\frac{dN}{d\eta}$ (middle), and $\frac{dN}{d\phi}$ (right) using one single event. Three event generators are used: ($\bullet$) HIJING, ($\circ$) CHIRAL, and ($\diamond$) VNI. The spectra of of $\frac{dN}{dp_T}$ and $\frac{dN}{d\phi}$ have the cut of $\mid \eta \mid= 2.5$ - 4.0.

emit several dozens of pions in a small range of azimuth, as well as in a small range of η. It is obvious that important physics is contained in the momentum spectra, and a device that fails to measure momenta would be seriously compromised.

The middle panel in Fig. 8 shows a relatively large dip at midrapidity for the single CHIRAL event. To be certain of this, the central TPC alone would not suffice. The portion of the spectrum in the FTPCs' η region is needed. The DCC may also lead to fluctuations in the azimuthal distribution of particles. The statistical uncertainties of the ϕ distribution on the right-hand panel of this Figure are unavoidable, but azimuthal resolution and statistical uncertainties from different binnings are a tradeoff to be optimized by an analysis.

Figure 10 addresses the question of stopping. Multiple-event ensembles from the three models discussed in the previous paragraph are compared with respect to measures of stopping. In the top panel, $dN/d\eta$ is shown for protons (with the anti-proton contribution subtracted). The HIJING and CHIRAL models are quite similar as would be expected. The redistribution of energy associated with the creation of simulated DCCs does appear to add a little extra stopping of protons, but the basic nature of the distribution remains the same. The parton cascade model is fundamentally different, as hard scattering processes underlying this model produce much larger stopping of the protons. Measurement of this effect needs

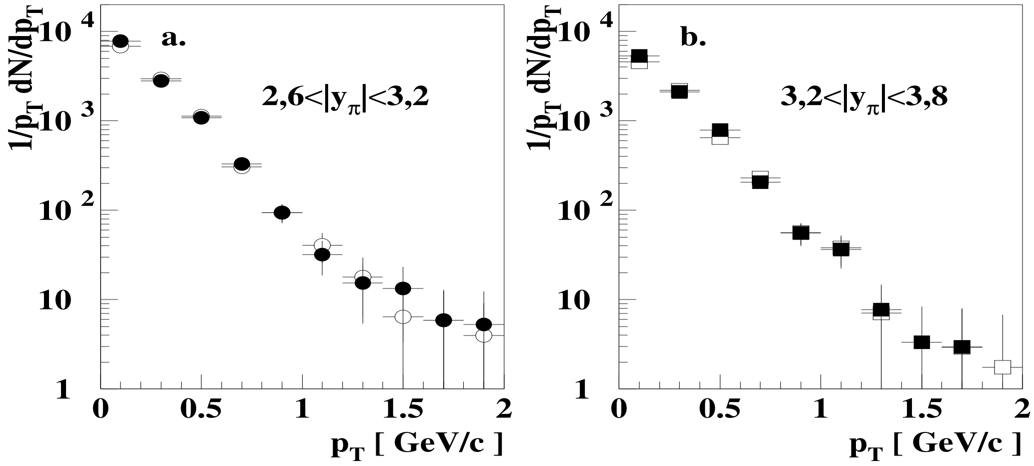

Figure 9: Transverse momentum distribution $1/p_T\ dN/dp_T$ for a single HIJING event for two rapidity intervals. Full symbols are for the generated event and open symbols are the results of tracking, reconstruction, and correction.

both the central TPC and the FTPCs. The FTPCs will not have sufficient particle identification capability to resolve protons, so we will use the $N(+) - N(-)$ analysis to assess the proton distributions. In the lower portion of Fig. 10 is shown the $N(+) - N(-)$ spectrum as function of η. It qualitatively reproduces the proton distributions on an event ensemble analysis. It will also be of interest to look at this as a function of momentum.

To achive the primary physics goals of the relativistic heavy-ion program which are associated with the properties of hot, dense matter, it is essential to have a fundamental understanding of the primary interactions of the incident nucleons and of the rescattering in the cold spectator matter. Therefore STAR needs to study p+A collisions as well. Characteristic features of p+p collisions determine the first collisions of p on A; they are fairly well known. Studies of p+A interactions add understanding of multiple interaction processes.

The acceptance of the baseline detector configuration is, however, not tailored to this study of asymmetric p+A reactions. Figure 11 illustrates this problem. The baseline configuration has tracking only up to $\eta \cong \pm 1.5$. The bulk of the particle flux is clearly outside this range. The particles at $y \approx 0$ (lab frame) are essentially those created in the first collisions of the beam proton and one of the leading nucleons of the gold nucleus. Figure 11 shows that it is more in the forward (with respect to the Au beam) rapidities that one becomes sensitive to effects of cascading through matter. The coverage of the FTPCs, in both η and p_T, allows one to study this rescattering-dominated region.

2.2.2 Peripheral Collisions

The FTPCs are very important in the STAR peripheral-collision program. This program includes two-photon interactions, photon-Pomeron interactions, and double-Pomeron interactions [kle97]. In all of the interactions to be studied, the photon or Pomeron couples coherently to the entire nucleus.

Because the photon and Pomeron are both colorless, these events are characterized by rapidity gaps. The final state of interest is visible in the central detector, with nothing else coming from the interaction. This contrasts with interactions, such as grazing nuclear collisions, beam-gas events and non-diffractive photonuclear interactions. The first of these is between barely overlapping nuclear skins. The second is mostly beam-hydrogen collisions. Both involve interactions which are hadronic and involve color exchange, and no gaps are expected. In the third case, i.e. a collision between a colorless photon and a colored gluon, there should be a rapidity gap on one side of the collision. Where colored particles are involved in the interaction, the phase space between the central rapidities and the beam nuclei should be filled with at least a few particles, producing tracks in the FTPC. In contrast, for the coherent interactions of interest, there should be no FTPC tracks coming from the interaction. Here, the relevant measure of acceptance is the total rapidity coverage; the two FTPCs have an acceptance comparable to the main TPC. Because of the high backgrounds at small radii from the beampipe, a simple scintillator veto would likely not suffice.

So, by selecting events where no FTPC tracks come from the interaction area, the event purity can be greatly increased. To quantify this, a Monate Carlo is necessary. We have simulated colored grazing nuclear collisions and beam-gas collisions using two event generators: FRITIOF and VENUS [kle95]. We have simulated photonuclear interactions with DTUNUC [nys97]. The results of this study are shown in Table 1.

	Grazing Nuclear Collisions	Beam-Gas	Photonuclear
FRITIOF	96%	94%	
VENUS	90%	90%	
DTUNUC			79%

Table 1: The fraction of simulated events that include at least one charged particle track in the FTPC acceptance. The input events were selected to already have a low multiplicity in the main TPC, and hence otherwise mimic central peripheral collision events.

Although the two Monte Carlo generators do not agree perfectly, the FTPCs should reduce grazing nuclear and beam-gas backgrounds by at least an order of magnitude. For photonuclear collisions, the rejection is somewhat lower because the photon is colorless, automatically leading to a rapidity gap. Still, the FTPCs can reject 3/4 of these events, without eliminating signal events.

The FTPC may also be useful for studying particle pairs produced diffractively in reactions such as $\gamma\gamma \to e^+e^-, \pi^+\pi^-$. These pairs may include electrons, muons, pions, kaons and protons. Diffractively produced pairs are produced with relatively small perpendicular momentum, and are hence likely to end up in the FTPC; the FTPC acceptance is e.g. 1.7% for such muon pairs. However, to select these events, some new trigger hardware that is sensitive to charged tracks in the FTPC acceptance would be required. Backgrounds also remain to be studied.

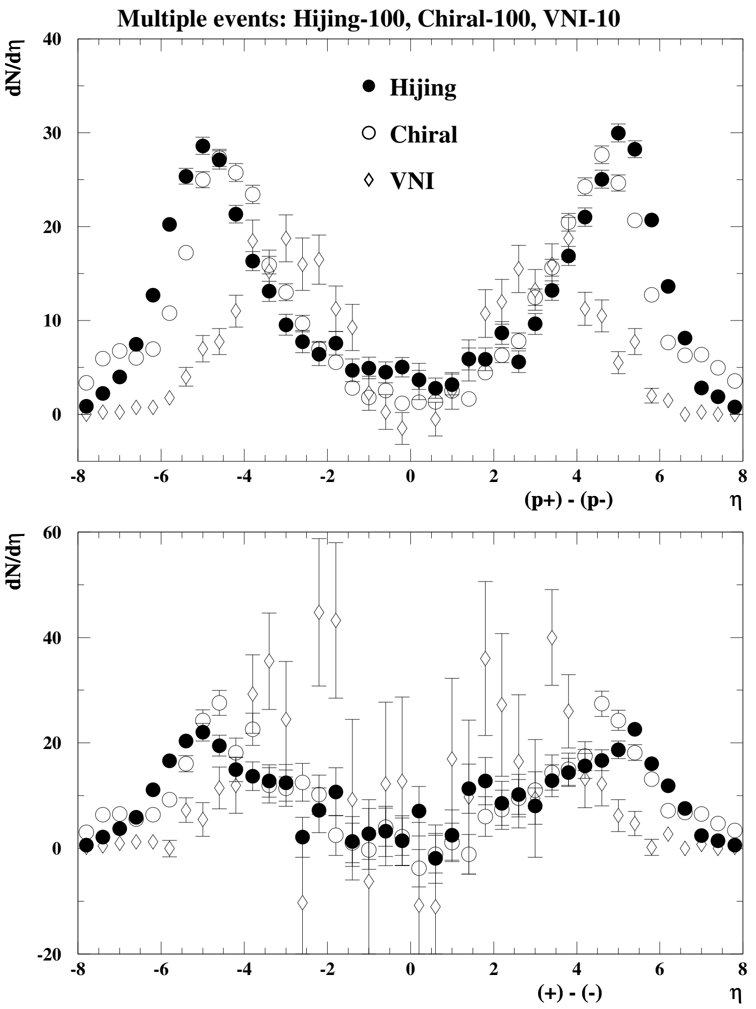

Figure 10: Pseudo-rapidity spectra for p–p̄ (top), and $N(+) - N(-)$ (bottom), respectively. A sample of events each from HIJING (• 100 events), CHIRAL (∘ 100 events), and VNI (⋄ 10 events) is used. Similar spectra based upon one single event are not shown because of excessive statistical errors.

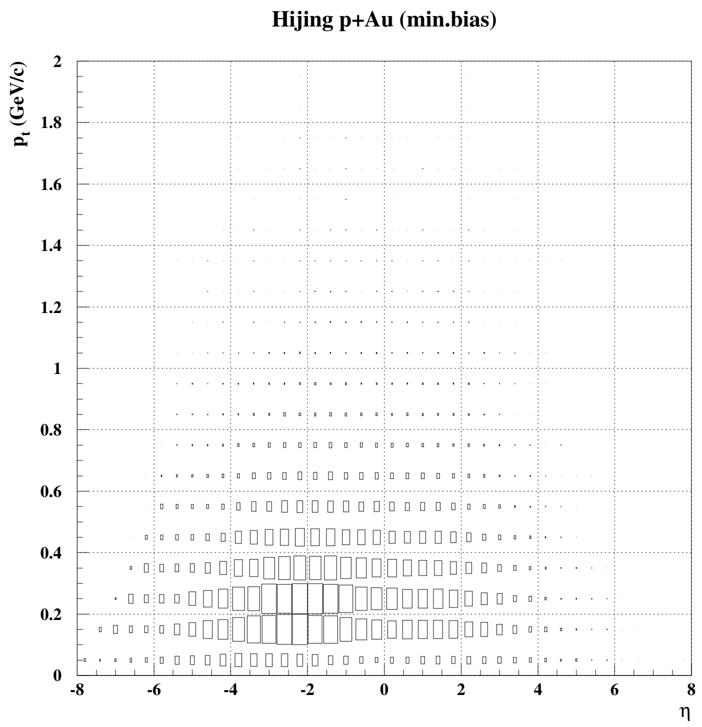

Figure 11: Phase-space distribution in (η, p_T) for p+Au collisions at RHIC in STAR.

3 Detectors

3.1 Research and Development Results

Substantial research and development was performed to optimize the design of the FTPC. The results of this effort led to the proposed set of design parameters which are documented in the following sections.

The requirement of high spatial resolution and good two-track separation using electrons drifting radially in a direction perpendicular to the magnetic field necessitated a careful search for a suitable gas for the FTPCs. Simulation of the electron drift in $\boldsymbol{E}$ fields or parallel $\boldsymbol{E}$ and $\boldsymbol{B}$ fields by the program MAGBOLTZ [bia89], agree fairly well with experiment for a variety of gases. However, with perpendicular $\boldsymbol{E}$ and $\boldsymbol{B}$ fields, the agreement for P10 gas is quite poor. Thus, this problem required considerable investigation, both experimentally [bit97] and theoretically [nes93]. Note that MAGBOLTZ expands the phase space of the drifting electrons in terms of Legendre polynomials (azimuthally symmetric) which are unsuitable in the presence of crossed $\boldsymbol{E}$ and $\boldsymbol{B}$ fields. Instead, the recently developed moments method [nes93] uses spherical harmonics which substantially complicate the mathematics, but give more accurate results for fast gases. The successful combination of both experimental and accurate theoretical investigation now permits a precise prediction of the FTPC performance with various gases, and allows interpolation between measured points.

Two FTPC prototypes, μSTAR and RTPC, have been built and studied. With μSTAR, we studied MSGC structures and gas properties relevant to diffusion and drift in a uniform electric field and also in a crossed magnetic field. With the radial-drift RTPC prototype, we studied the particular features associated with diffusion and drift in a radial $\boldsymbol{E}$ field with a crossed $\boldsymbol{B}$ field. More information is available in Ref. [bit97].

3.1.1 Measurement of Gas Parameters in $\boldsymbol{E}\perp\boldsymbol{B}$ Fields with μSTAR

Figures 12 and 13 show both measurements and calculations [bit97] for the transverse and longitudinal diffusion coefficients, the drift velocity, and the Lorentz angle for a uniform $\boldsymbol{E}$ field. These are for Ar-CO_2(50%), the gas which is presently favored for the FTPCs. A magnetic field of $B = 2.4$ kG was chosen due to an experimental constraint. The points were measured for a uniform electric field with a perpendicular magnetic field, using μSTAR. For this cool gas, they are in good agreement [bit97] with both MAGBOLTZ [bia89] and the moments method [nes93]. This result was expected since Ar-CO_2 has low diffusion coefficients, small Lorentz angles, and little sensitivity to the $\boldsymbol{E} \perp \boldsymbol{B}$ effect.

3.1.2 Electron Transport in a Radial-Drift TPC with Axial B Field

Figure 14 presents measurements [bit97] of electron-cluster properties as a function of drift distance for Ar-CO_2(50%). The radial-drift RTPC chamber was operated at a drift voltage of 15 kV in a perpendicular magnetic field of 5 kG. Because the electron clusters drift in a non-uniform electric field, we can not directly compare the transport parameters with calculations. Instead, we compare cluster properties measured at the readout radius with those calculated by propagating the cluster through the non-uniform $\boldsymbol{E}$ field to the readout radius, using our measured gas parameters for a uniform $\boldsymbol{E}$. The black dots show measured quantities such as drift time (μs), deflection angle (defined as the Lorentz angle integrated over the drift length in the radial field), azimuthal width, σ_ϕ (mm), and radial width, σ_r (μs). Fig. 15 presents the cluster properties as a function of the magnetic field for a fixed drift distance (d = 27 cm), again for Ar-CO_2(50%). The drift time and azimuthal and radial widths are almost independent of the magnetic field up to 7.5 kG. Fortunately, the perpendicular magnetic field has a minimal effect on drift velocity and diffusion width for this cool gas. Overall, we find good agreement between measurements and calculated transport quantities for an electron cluster in a radial $\boldsymbol{E} \perp \boldsymbol{B}$ field.

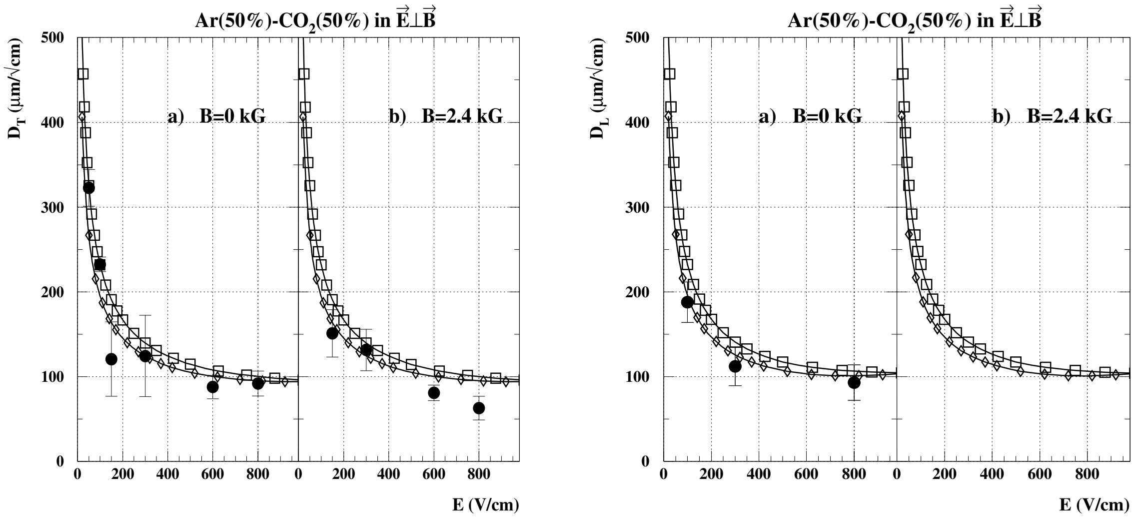

Figure 12: Transverse (left panel) and longitudinal (right panel) diffusion coefficients as function of the drift field for : (a) $B = 0$ kG; (b) $B = 2.4$ kG. The plots show data points (•), calculations using the moments method (□), and calculations using the Magboltz program (◇); smooth curves were drawn through the calculated points.

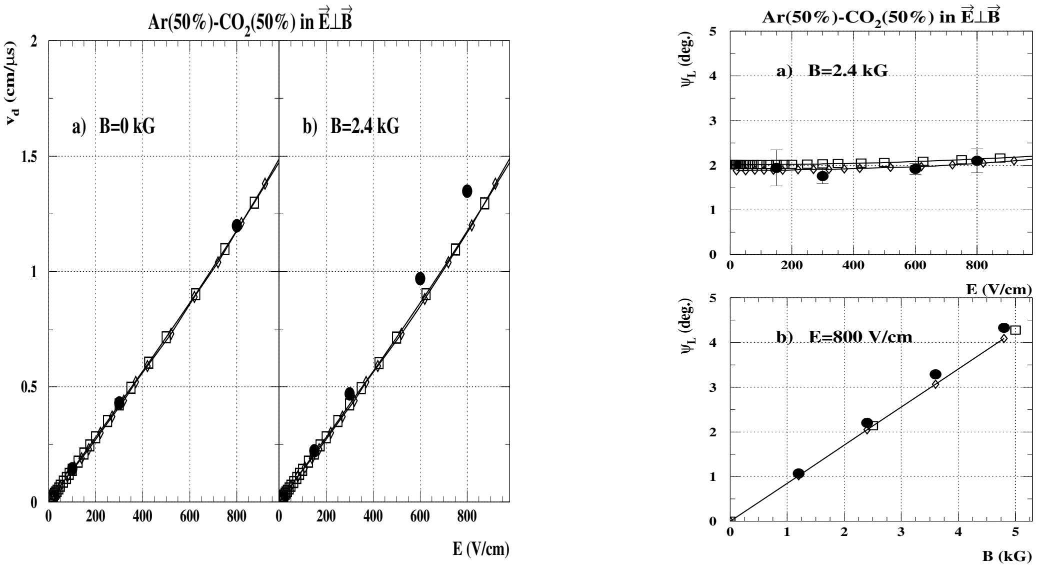

Figure 13: Drift velocities (left panel) as a function of the drift field for : (a) $B = 0$ kG; (b) $B = 2.4$ kG. Lorentz angles (right panel) (a) as a function of the drift field for $B = 2.4$ kG; (b) as a function of the magnetic field for $E = 800$ V/cm. The plots show data points (•), calculations using the moments method (□), and calculations using the Magboltz program (◇); smooth curves were drawn to connect the results of the calculations.

3.2 Detector Design

3.2.1 Conceptual Detector Design Parameters

The specification of the design parameters is driven by the physics requirements. In order to determine the primary particle distribution, it is necessary to be able to detect all particles, and reject those which are the result of secondary interactions in the beam pipe or other surrounding materials. Also one requires a two-track separation of a few mm at high η where the particle densities are the highest. Besides the good tracking efficiency, a precise position measurement is needed for the charge and momentum determination. Both can be achieved in the available volume by using a low diffusion gas, a matching segmentation in the readout chambers and a well adapted front-end electronics.

There are two chambers, one on each side of the collision point. The sensitive gas volume of each chamber has an inner radius of 8 cm, an outer radius of 31 cm, and a length of 120 cm. It will be positioned at $|z| = 150$ to 270 cm. See also Figs. 2 and 16.

Our studies [bit97] show that both Ar-CO_2(50%) and Ar-DME(50%) are suitable gas mixtures for this FTPC. Both mixtures have small diffusion coefficients of about

100 μm/$\sqrt{\text{cm}}$. The CO_2 mixture is a factor 2 faster than the DME mixture. The Lorentz angle for the CO_2 mixture (about 4 degrees) is also twice as large as that for the DME mixture. The required drift fields should range between 240 and 1400 V/cm. The optimal drift cathode voltage depends on the choice of gas mixture. As the Ar-CO_2(50%) gas mixture is faster, nonflammable, and less demanding in construction material, it is preferable to the Ar-DME(50%) gas mixture. A drift voltage of 10 kV would provide a drift field ranging from 240 V/cm at the outer radius to 920 V/cm at the inner radius.

Each FTPC has 10 pad rows. One row is divided into 6 azimuthal sectors containing 160 pads each. The pads are 20 mm long parallel to the beam and have a pitch of 1.9 mm azimuthally. This segmentation results in about 20.000 readout channels in total. Due to the use of the "cool" Ar/CO_2 gas mixture the electron drift velocity is low. This allows a long shaping time and time-bin size, 400 and 200 nsec respectively, and a sampling rate of 5 MHz. For the 50 μsec drift time, 256 time bins provide enough resolution. This way the amount of data to be recorded is optimised to a minimum. The design parameters are listed in Table 2.

3.2.2 Detector Description

A schematic drawing of the detector is shown in Fig. 16. The basic structure of each FTPC is an aluminium cylinder of 1200 mm length and 728 mm diameter with 30 openings for the readout sectors. Five sectors are in a row in beam direction, containing 2 pad-rows each, and are subdivided into 6 sectors in ϕ direction. Within one readout sector the pad-row separation is 65 mm and from sector to sector it is 108 mm. The dead area between adjacent sectors is 16 mm wide in azimuth which represents less than 5% loss of acceptance. The cylinder is closed with 100 μm thick Mylar foils at both ends. Five front-end electronic boards are mounted on each readout chamber and are covered by a cooling plate (see also 5.3). Flat cables run on the outer surface to the readout boards behind the FTPC. A finite element analysis of the complete cylinder (without the support), including the weight of the readout chambers, electronics, cables etc., gives a vertical deformation by gravity of less than 100 μm.

The complete detector is supported and positioned by 4 bars connected to the inner field cage ring of the central TPC. The radial field is established by a tube around the beam pipe, at negative high voltage, and the readout chambers at ground potential on the outer wall of the cylinder. At the ends, the radial field is defined by a plane of 17 concentric toroidal potential rings, made of Al tubes with 300 μm wall thickness, and a corresponding resistor divider chain. The rings are supported by six ceramic bars, as shown in Fig. 17.

Table 2: FTPC design parameters

PARAMETER	VALUE
Configuration	
# of TPC	2
# of pad rows per TPC	10
# of sectors per pad row	6
# of pads per sector	2×160
Volume	
inner radius	8.0 cm
outer radius	31.0 cm
chamber length	120.0 cm ($\|z\| = 150 - 270$ cm)
acceptance	η=2.5 - 4.0 (θ=2.0^o - 9.3^o)
Field	
drift cathode voltage	10-15 kV
drift electrical field	240-1400 V/cm (radial, $\perp$ beam)
solenoid magnetic field	0.5 T ($\|$ beam)
Gas	
gas mixture	Ar(50%)-CO_2(50%)
drift velocity	0.3 - 2.0 cm/μ s
trans. diffusion D_T	100-130 μ m/$\sqrt{cm}$
long. diffusion D_L	100-130 μ m/$\sqrt{\mathrm{cm}}$
Lorentz angle	4 deg.
gas gain	$\sim$ 1-2$\times 10^3$ (gain doubling per $\Delta V_a = +100$V)
Readout	
total # of pads	$\sim$ 19200
# of time bins per pad	256
pad pitch	$\sim$ 1.9 mm
pad length	20 mm
pad capacitance	$\sim$ 10 pF
shaping time (FWHM)	400 ns
SCA sampling rate	5 MHz
SCA time bin size	200 ns
ADC dynamic range	8 bits

For the two critical items, the tube-like HV-electrode and the potential rings, mock-ups have been tested. For the former, a short HV insulator made of 3 mm thick plastic material (ABS) was covered inside with a conductive layer to simulate the ground potential close to the beam pipe. The outside was covered by another conductive layer where the HV was applied. This setup held 25 kV for a week without problems, which is approximately twice the field strength required in the experiment. For a test of the potential rings, a structure with 8 rings of 10 mm diameter tubes and 3 mm distance between tubes was tested under gas. In the inner region (highest $\boldsymbol{E}$ field), a sustained electric field strength of 4 kV/cm was obtained, a factor ~ 3 higher than needed. The field was applied for several days without discharge problems.

3.2.3 Readout Chambers

One readout sector covers 60° in ϕ and contains the 320 pads of two pad rows. The inner surface is curved with a radius of 305 mm while the mounting flange is flat for easier machining and sealing. Only the amplification structure, wires or anode strips, are in front of the pads. The other necessesary electrodes, the ground electrode (Frisch grid) and gating grid are independent from the readout chambers and mounted to the inner surface of the detector cylinder.

The original preference for readout was to use MSGCs because of their intrinsic high resolution and the possibility of constructing curved anode strips perpendicular to the pad direction. Various strip structures have been investigated experimentally, and the production method for glass bending has been developed and tested. However, recent investigations [boi97] indicate a limited MSGC lifetime in the presence of heavily ionizing particles at the MSGC surface. They induce micro-discharges which destroy the thin anode strips. This effect needs more investigation and therefore the use of MSGCs was dismissed.

A more conventional method with short wires crossing the pads at a relative small angle with respect to the axial directions has been tried as an alternative. Such a geometry allows also the construction of curved chambers (see also Fig. 2). When at least 2 wires cross a pad, the usual pad response function (PRF) is recovered. (In the case of 0° the pad response function is distorted by the wire distance leading to systematic deviations in the cluster position measurement.) Measurements with a flat chamber having 2 mm distance between sense wires and pad plane, 2.5 mm pad pitch, and 20 mm pad length have been performed for 0°, 9°, 16°, and 90° crossing angle. The above mentioned distortion disappeared for the 9° angle, and the result is comparable with that of 90°. With a curved prototype chamber in the RTPC with a gap of 1.7 mm, 1.9 mm pad pitch, and a 17.4° crossing angle, stable operation up to high amplification in Ar/CO_2 (50/50) has been obtained and no distortion has been observed. The impacts from a laser beam with less than 1 mm diameter were mainly 4 pads wide. Therefore we will reduce the gap between sense wires and pad plane by a few tenths of a mm giving a narrower PRF and a better position measurement and two-track resolution. The position measurement accuracy was determined from the distribution of 500 laser tracks to be 140 μm. This is an upper limit because it includes possible position fluctuations of the laser beam. Taking this effect into account and assuming the narrower PRF, a position measurement accuracy of about 100 μm can be expected.

Most of the parameters used for the simulations are independent of the readout principle. The only exception is the width of the pad response function which influences the two-track resolution in ϕ direction. It will be approximately 50% larger for the wire chamber solution. But the effect is nearly negligible for tracks produced close to the beam pipe, where the particle density is highest. There, the resolution is determined by the electron diffusion and the widening of charge clusters due to the radial drift. For tracks in the outer region, for which the pad response function dominates the 2-track resolution, the particle density is much lower and the reduced resolution of the wire chamber is adequate. However, the readout sectors are designed in a way that a later change to MSGCs is possible, for example as an upgrade.

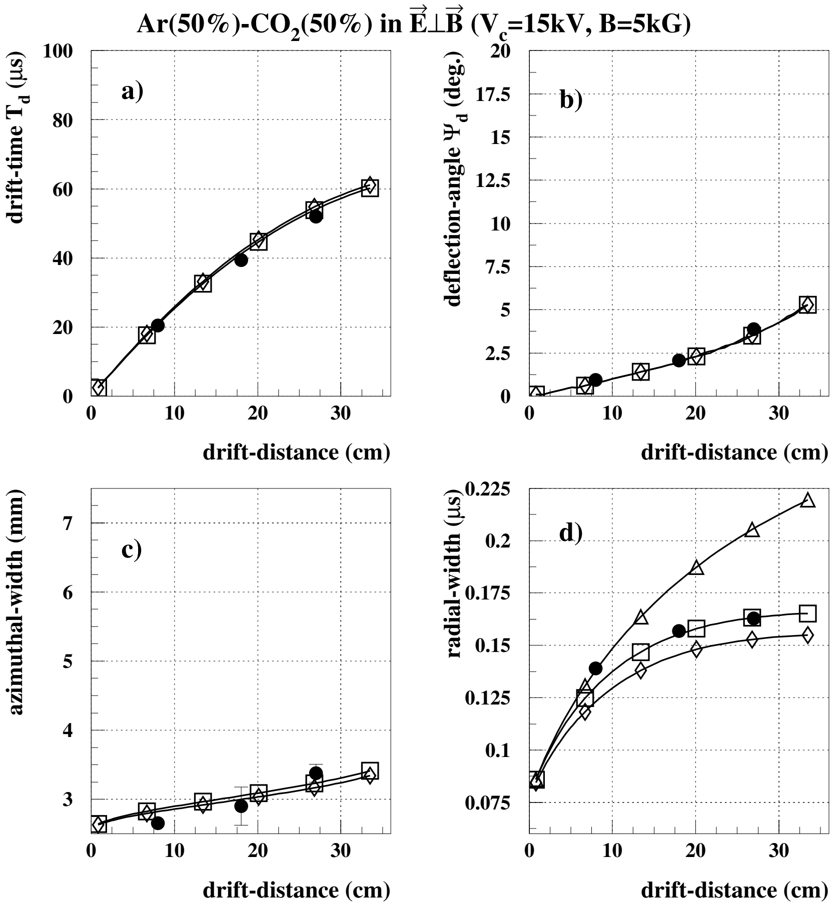

Figure 14: Electron-cluster properties a function of drift distance for the RTPC prototype: (a) drift time (μs); (b) deflection angle (degree); (c) azimuthal cluster width σ_ϕ (mm); and (d) radial cluster width σ_r (μs). The plots show data points ($\bullet$), calculations using the moments method ($\Box$ with and $\triangle$ without the $\partial v/\partial r$ term in Eq. (7) of Ref. [bit97], and calculations using the Magboltz program ($\Diamond$); smooth curves were drawn to connect the calculated values.

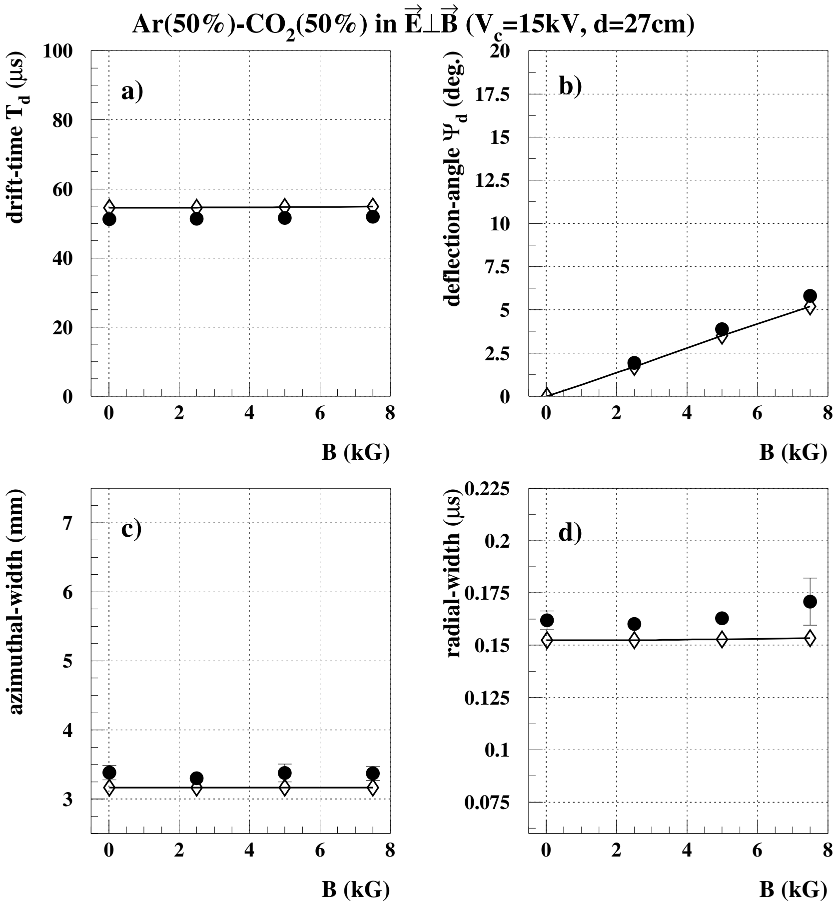

Figure 15: Electron cluster properties as a function of the magnetic field inside the RTPC prototype: (a) drift time (μs); (b) deflection angle (degree); (c) azimuthal cluster width (mm); and (d) radial cluster width (μs). The plots show measured data points ($\bullet$), and calculations using the Magboltz program ($\diamond$); smooth curves were drawn to connect the results of the calculations.

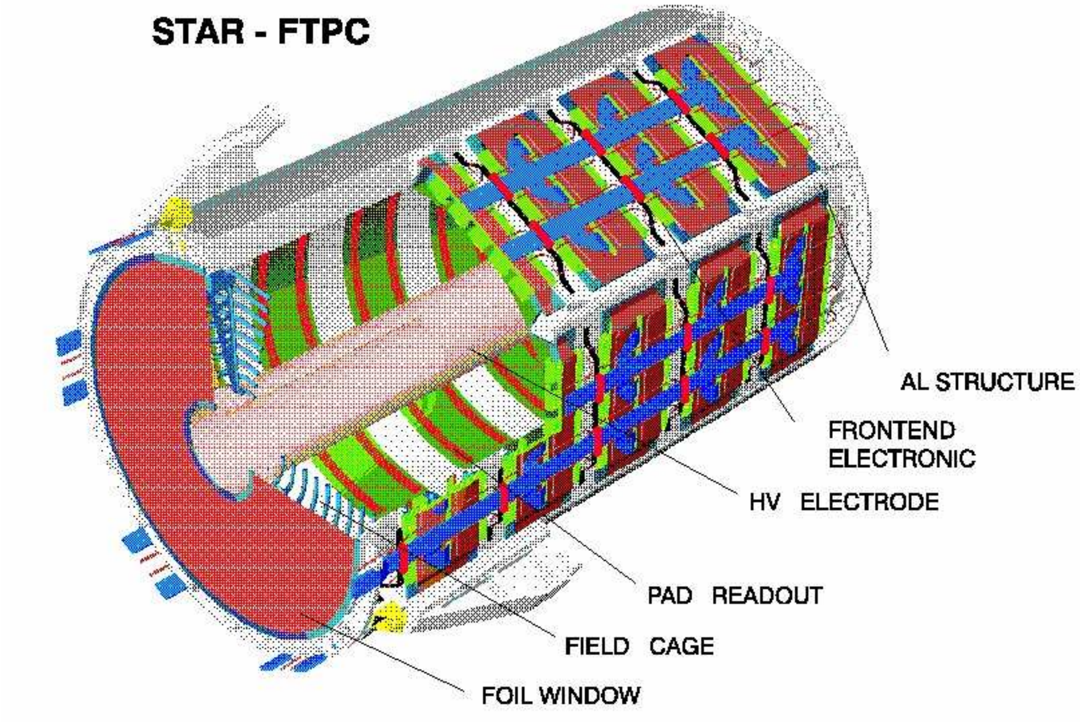

Figure 16: Structure of cylindrical FTPC.

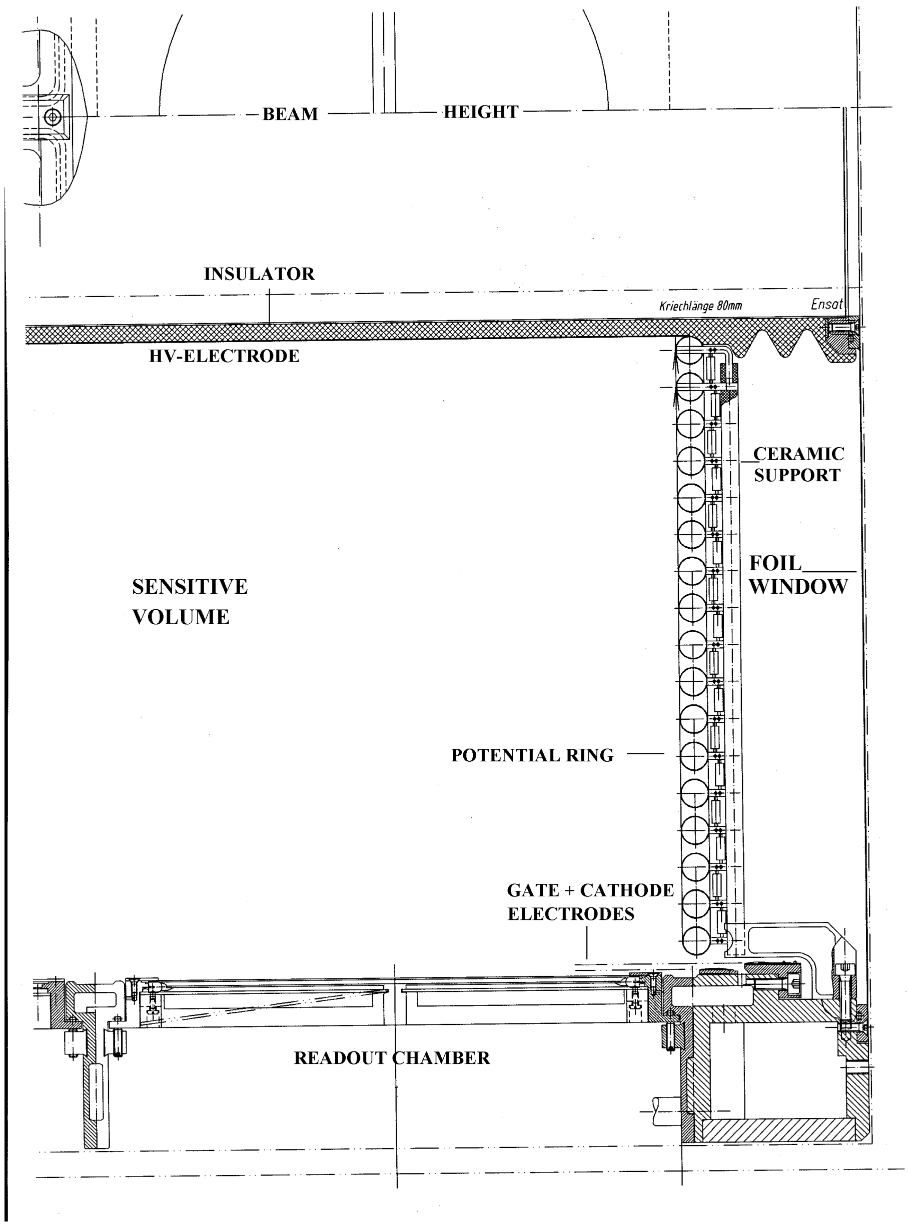

Figure 17: A radial cross section of the FTPC detector showing the ceramic supports of potential-forming ringshaped tubes.

4 Electronics and Data Acquisition

4.1 Front End Electronics

4.1.1 Requirements

Each detector has about 10,000 pads. Therefore two FTPCs have 20k channels of electronics, capable of measuring time samples. The drift length of 23 cm (48 μsec) is subdivided into 256 time bins. For slow drift gas a rise time of 350 nsec (400 nsec FWHM pulse width) is used. The sampling rate is 5 MHz.

Simulations show that the required position and momentum resolution can be obtained with a mean signal to noise ratio of 20:1 (mean value). Taking into account a factor of 4 for tracking $Z = 2$ particles, and allowing for fluctuations of a factor of two, leads to the requirement of a dynamic range of 1:160. A 10-bit ADC is more than adequate for this task, and reduction to 8 bits via software translation tables will not impact the quality of tracking and momentum resolution.

4.1.2 FEE Description

The FTPC front-end electronics closely follow the electronics [bet96] of the central TPC. A block diagram is shown in Fig. 18. Each pad is read out by a low-noise STAR preamplifier/shaper (SAS), which sends signals to a switched capacitor array/ADC chip (SCA/ADC). For the FTPC, four chip sets handling 64 channels will be mounted on a small FEE card, which will plug directly onto the detector. The SAS chips also have a built-in calibration system which can monitor electronics gain. Eighteen FEE cards will be read out by a readout board, which sends the signals over a 1.2 Gbit/sec fiber-optical link to the data acquisition system. The readout board also controls the FEE cards, based on signals from the clock and trigger distribution system and the slow control links. Both of these interfaces are almost identical to those in the main TPC system. The entire FTPC system can be read out at 200 Hz, as the main TPC.

Although the same design is used for the main TPC and the FTPC, several of the electronics parameters are externally set differently. The SAS shaper is set to have a FWHM of 400 nsec, about twice that in the main TPC. The $1/t$ tail correction circuit time constant may also be adjusted. These changes are made by changing control voltages that feed into the SAS. Only 256 time bins are used in the SCA, and the sampling rate of 5 MHz is slower than in the main TPC. Because the SAS time constant is increased, the output slew rate is similarly decreased. This will allow us to reduce the current in the SAS output buffer (also programmable), reducing the overall SAS power consumption by about 60%. This directly translates into a reduced cooling requirement.

Although the electrical design is almost unchanged from the main TPC, the

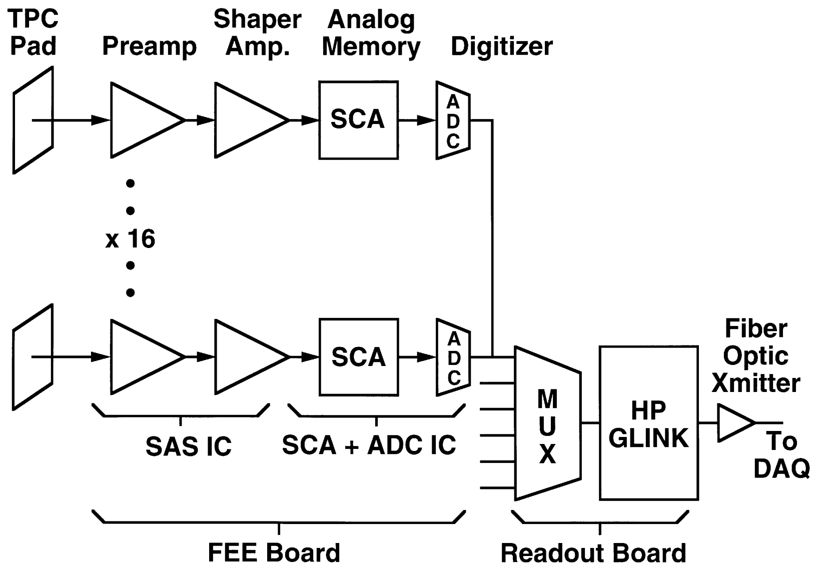

Figure 18: Block diagram of the FTPC electronics. Signals from the TPC pads are fed into the SAS chip which amplifies, shapes and buffers the signals, and then into the SCA/ADC chip, which stores 256 time bins and then digitizes them to 10 bits. One readout board multiplexes signals from 1152 (=18 $\times$ 64) pads and sends them to the data acquisition system over a single fiber optic cable.

mechanical layout is quite different. In the FTPC, space is considerably more limited than in the main TPC. The 64-channel FEE cards will be mounted directly on the chamber and, in contrast to the main TPC, parallel to the readout chambers. This leaves very little volume for mounting the components. The SAS and SCA ICs will be packaged in 80- and 100-pin plastic quad flat packs with the smallest possible footprints. The readout board will be mounted behind the chamber (in the beam direction, away from the interaction point). A new PC board layout will be required to fit in the available space.

The slow controls and triggering systems will be identical to the main TPC. The power supplies, cables and controls will also be identical to those used in the main TPC. FTPC cabling is included in the STAR integration plan; cables starting on the platform are routed following the main TPC cables, and then down the TPC wheel to the FTPC.

4.2 Data Acquisition

4.2.1 Introduction

Since the design of the readout electronics of the FTPC is kept as close as possible to that of the TPC of the STAR Detector, the same strategy is followed for the DAQ system of the FTPC. For the connection to the event builder, the FTPC will be treated as a separate subdetector.

In the following discussions of the FTPC DAQ system, we will concentrate on these requirements and describe the differences to the TPC readout.

4.2.2 Data load

The total number of readout channels for the two FTPCs consists of 20000 channels. Each readout channel (pad) has a depth of 256 time bins, which leads to a raw data volume of 5.5 MByte per event after conversion of the 10-bit ADC values to 8 bits.

The event size depends strongly on the beam pipe material, since scattering processes in the beam pipe result in different occupancies of the detector. The standard beam pipe contains much steel which leads to an occupancy of 23%. Simulations show that for a beryllium beam pipe the occupancy would decrease to 13%.

Table 3: Event size and Data volume for the two different beam pipe designs:

Beam pipe	number of channels	Event Size [MByte] (raw data + 30% for data format)	Raw Data volume (25 events/sec) [MBytes/sec]	Cluster event size (for 100 events/sec) [MBytes/sec]
Steel	20 000	1.64	41	40
Berrylium	20 000	0.93	23	24

Table 3 shows the influence of the two different beam pipes on the total data volume. Column 2 shows the zero-suppressed ADC event size plus 30% for the data format. Column 3 shows the zero-suppressed ADC data volume for a throughput of 25 events per second. Column 4 shows the throughput for the case of 100 events per second, where the ADC data have been replaced by cluster (space point) information. These calculated values allow the reader to estimate the impact of running at different trigger rates in the baseline mode [cluster information is passed to the sector level 3 trigger at rates of 100 Hz, with events built from zero-suppressed ADC data] or an alternate mode [zero-suppressed data are passed to a later processing stage at somewhat reduced rates].

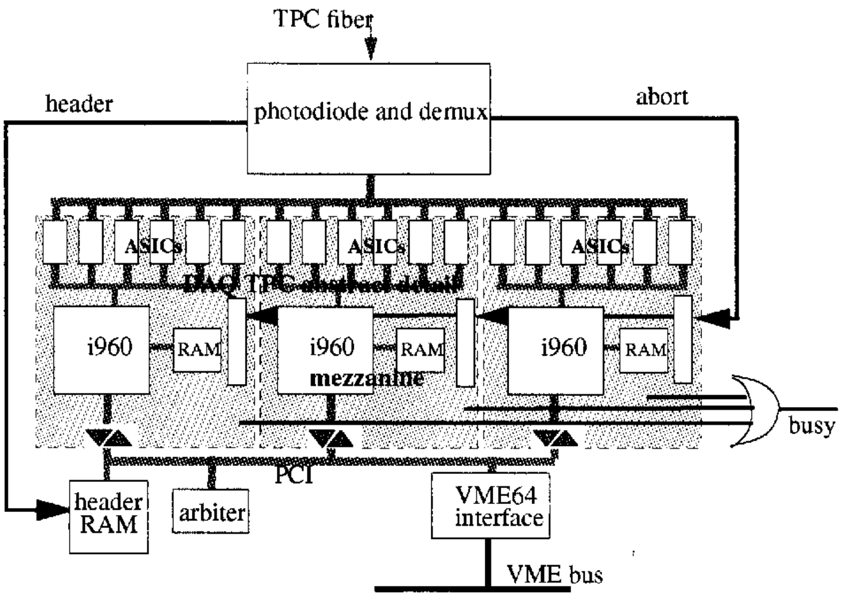

Figure 19: DAQ receiver board.

4.2.3 Readout crates

The readout crates have the same functionality as the TPC sector crate and will have a similar setup as in the TPC case.

Each receiver board gets data of 1152 pads, which are distributed to 3 PCI mezzanine boards (see Fig. 19). On each PCI mezzanine card are 6 ASICs responsible for pedestal subtraction and hit finding. Cluster finding, as well as structuring and packing of the data, will be done on an i960 processor.

Each readout crate is controlled and managed by a crate broker CPU. Its responsibility is allocation of resources for each event in the crate and communication to CPUs outside of the readout crate. We plan to put 12 receiver boards into one readout crate (see Fig. 20), which is sufficient to read out one FTPC chamber.

4.2.4 Third level triggering

As in the case of the TPC, we want to provide the possibility for the FTPCs to participate in the trigger decision of the third level trigger. For the hardware implementation it should be kept in mind that the FTPCs contribute a substantial part of the event size (see Table 3). It is thus essential to limit the number of pads processed by a single receiver board to 1152. It is unlikely, however, that for 12 receiver boards 2 L3 sector CPUs will provide enough CPU power for third level

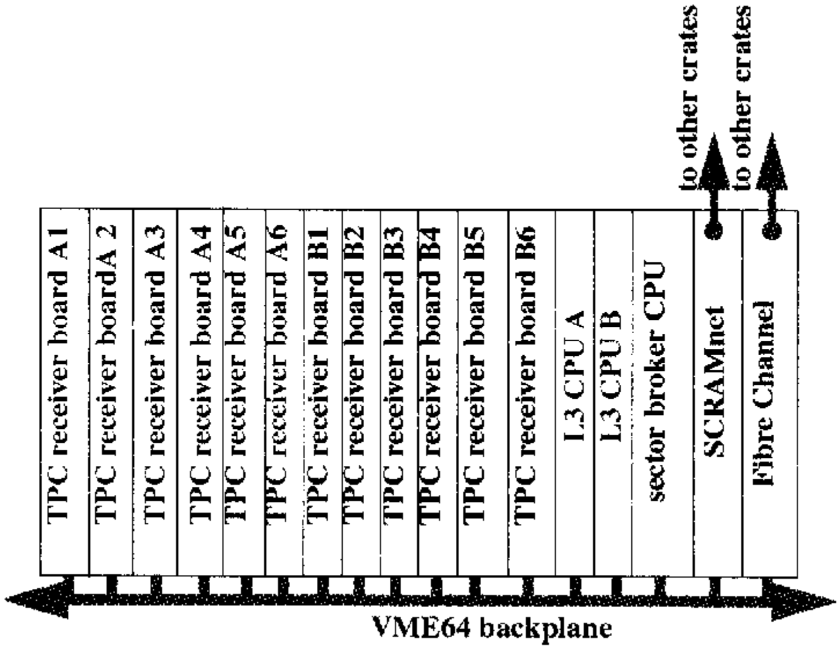

Figure 20: DAQ sector crate.

triggering.

5 Simulation and Tracking

To document the FTPC performance given the proposed design parameters, a simulation chain was set up to perform the following:

- Tests of the FTPC tracking algorithm for its ability to find primary tracks traversing the FTPCs, and to reject most of the non-primary tracks at track densities up to three per cm^2.
- Studies of momentum resolution and charge determination of primary particles traversing the sensitive volume of the FTPC.
- Determining the capabilities to measure distributions of pseudorapidity, rapidity, p_T and differences of spectra of positive and negative tracks $(N(+)-N(-))$ using "realistic" events from various event generators.
- Assessing the possibility to distinguish between different physics models.

5.1 Simulation Chain

A complete FTPC simulation chain has been set up in the STAF framework. This is described in the PhD thesis of Michael Konrad [kon97]. In Fig. 21 the parts of the FTPC simulation chain are illustrated. The shaded boxes indicate the parts of the chain which are implemented as *Physics Analysis Modules* (pams) in STAF.

In addition to the pams in Fig. 21, a module (fpe) for dE/dx investigation has been developed and a stand-alone version of an FTPC slow simulator is presently being converted into a pam. The slow simulator takes the GSTAR hit coordinates, follows the drift and diffusion, and produces a distribution of charge over space (pads) and time at the pad plane. Finally, the pad response function and the electronic response are simulated.

5.2 Tracking in FTPCs

One of the most challenging tasks for the FTPC software has been the development of a set of algorithms which reconstructs the tracks of most of the primary particles passing through the FTPCs and rejects the majority of the non-primary tracks (from decays, γ conversions, showers etc.). With a maximum of ten measurements on a track, the FTPC has to cope with track densities up to three per cm^2, as illustrated in Fig. 22. The description of the method will be slightly schematic, for the purpose of brevity and clarity of the main ideas, and will not match exactly Fig. 21.

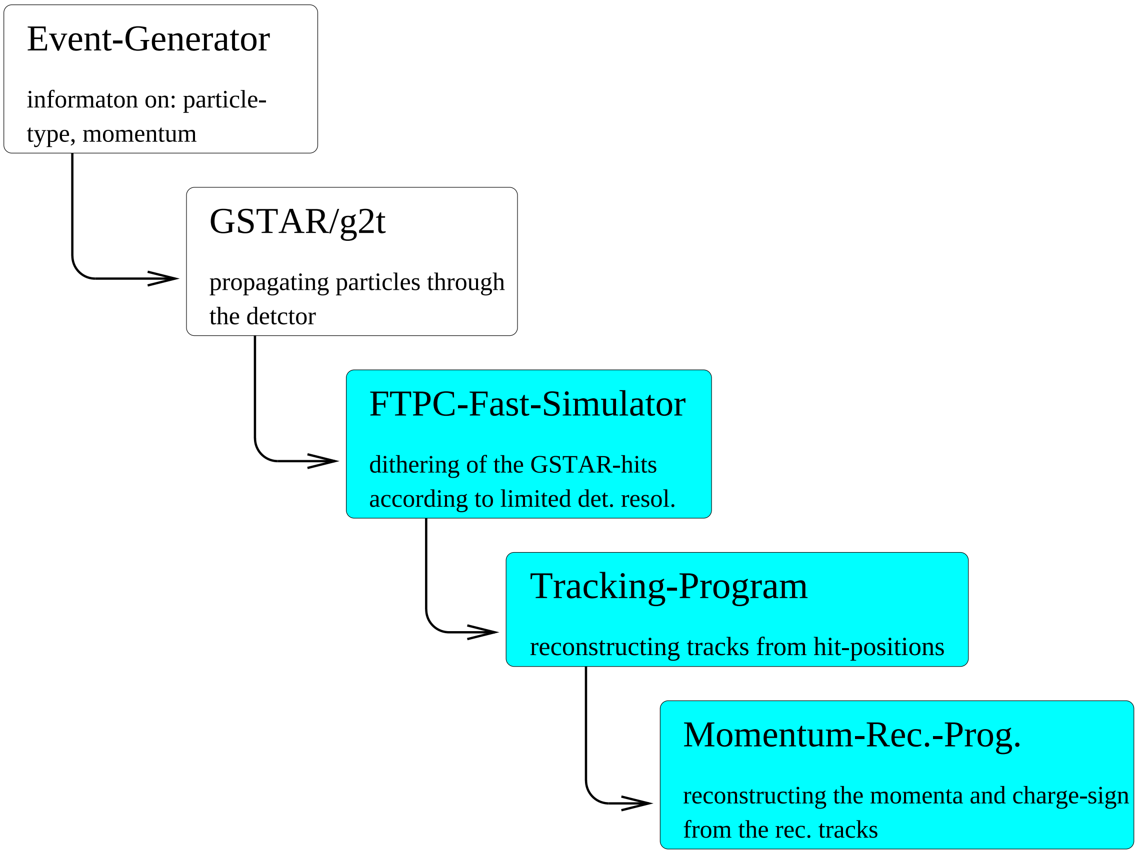

Figure 21: FTPC simulation chain

5.3 Tracking Algorithm

Figure 23 shows the variables pertinent to the FTPC tracking algorithm [dra95]. It is based on a helical trajectory for a particle from the interaction point (IP) to and through the FTPC. It is known that the magnetic field in the region of the FTPCs is not entirely uniform, hence the actual tracking has been done with a realistic magnetic field map; the efficiency of the algorithm does not suffer from the small expected deviations of trajectories from a helix. The tracking deals entirely with projections in the x, y plane (z direction is parallel to the RHIC beam, with the origin of the coordinate system in the interaction point).

The circle in Fig. 23 starting at the vertex and passing near (x_1, y_1) and (x_n, y_n) is the projected helical trajectory. The hits in the planes (only 7 are shown here for economy of space) are the stars, which are not exactly on the circle because of diffusion, etc. The angle between the line through the vertex and (x_1, y_1) and the line through (x_1, y_1) and (x_n, y_n) is defined as the twist angle τ. For a helical

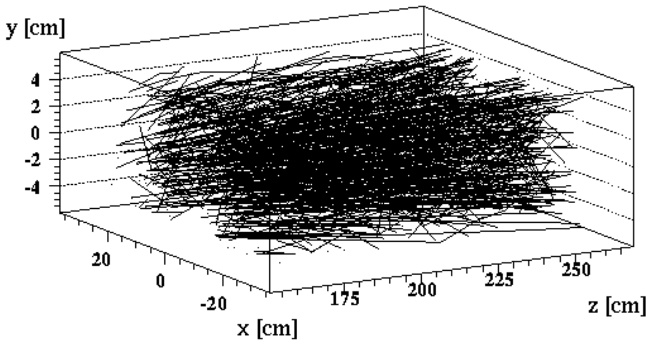

Figure 22: Tracks from one central Au+Au collision in a portion of one FTPC

trajectory, the twist is exactly inversely proportional to the longitudinal component of momentum. For $\eta > 2.5$, this longitudinal component is within 1.3% of the total momentum p, so for conceptual purposes (not for exact calculations) one can approximate the twist angle by $\tau = K/p$. The quantity $K = 0.15\ z_n B$, where z_n is the longitudinal position of the last hit plane of the detector, and B is the uniform longitudinal field strength. For a track passing through the full length of the TPC, $K = 0.203$ GeV/c for $B = 0.5$ Tesla, giving the twist in radians. Since the $\boldsymbol{B}$ field is not perfectly uniform, the exact helical relation becomes slightly dependent on the polar angle θ which defines pseudorapidity. However, since K is evaluated from GSTAR simulations with a realistic $\boldsymbol{B}$ field map, part of this dependence is removed by choosing a θ dependent value of K slightly different from this analytic value for a uniform $\boldsymbol{B}$.

The relation, $\tau \cong K/p$, is the key to the measurement of momentum in the FTPC. The qualitative fact that the two lines that define twist in Fig. 23 are much farther apart near the center of the chord than the length s of sagitta is the basic reason why momentum determination from twist is more accurate than from curvature for the FTPC for all but the very smallest momenta.

For determining pseudorapidity, the polar angle of the particle is

$$\theta = \arctan\left((r_n/z_n)(\tau/\sin\tau)\right)\ , \tag{1}$$

where r_n is the radius of the last hit, viz., the distance in Fig. 23 from the vertex to the point in the helix nearest to (x_n, y_n). For small τ the angle θ is the obvious geometric one. As τ increases, θ is increased by the factor $\tau/\sin\tau$ from the bending by the field.

Thus, the z component of momentum p_z is determined directly from the twist τ, and θ is determined directly from the measurables, r_n, z_n and twist τ. The

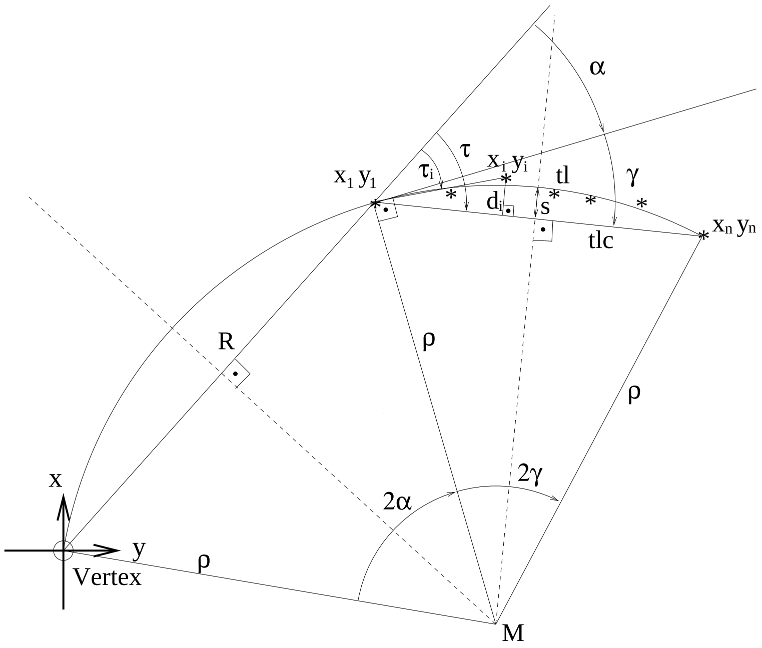

Figure 23: Variables for the tracking algorithm.

total momentum is then given by $p = p_z/\cos\theta$ and the transverse momentum by $p_T = p_z \tan\theta$.

Next one makes use of the fact that for primary tracks there is a relation between the quantities: twist τ, first-hit position R, and track length (tlc in Fig. 23). The set of hits from a primary track must satisfy this relationship within some tolerance reflecting diffusion, multiple scattering in the beam pipe, etc. Other hits are rejected as due to non-primary tracks.

Consider now the method of recognizing a track. A hit in the first plane is selected. Its R determines the track length tlc for a given twist. Then a zone in the last plane, at the distance tlc from the first hit for each possible τ, is searched for a hit that would have the correct combination of tlc and τ. Finding a hit with a correct combination of tlc and τ determines a tentative value τ, and thus, the position of a tentative center of curvature M with its associated tentative radius of curvature, ρ. One has therefore a candidate for a circular track; hits from the other planes must be close to it. If there is a sufficient number of hits close enough, a primary track is declared found, and the corresponding hits are removed from the pool of hits. Note that the third coordinate, z, is implicitly included in the algorithm as each plane is at a given z.

Next arises the question of the optimal determination of momentum based on all hits. For this, the residual distances between the circle centered at M and the hits are determined. Then a linear least-squares fit is done to find the "slope" of the best line through these residuals. If this "slope" is non-zero, the tentative twist is corrected by the angle of this "slope" to give the best twist for all hits.

The interaction vertex can be determined approximately from any acceptable track. This is done by [kon97] tracing the track backwards to the point of closest approach to the beam axis. The resulting uncertainties estimated from GSTAR simulations of Au+Au collisions are about 50 μm in x and y, and about 0.8 cm in z.

The sign of the charge is easily determined. It is the same as the sign of the twist angle.

It should be mentioned why the FTPC is placed inside the STAR solenoid. If it were outside, with no additional magnets, the twist angle would vanish, and there would be no way to measure momentum. This is because the effect of the full radial $\boldsymbol{B}$ just cancels [dra95] the twist produced by the axial component of field. This is true at any radius of passing through the field.

6 Expected Performance of FTPC

6.1 Introduction

Using the measured gas parameters, we evaluated the expected cluster parameters inside the FTPC by using Eqs.(5)-(12) from Ref. [bit97]. It is assumed that a primary track originating from the collision vertex generates one cluster per pad row. Fig. 24 shows, as a function of the radial position of the hit, the cluster properties, i.e. total drift time (T_d in μs), total deflection angle (Ψ_d in degree), single cluster width in pad direction (σ_{pad} in mm) and in time direction(σ_{tim} in μs), and two-track resolution (two clusters separated by 3σ) in radial direction(σ_r in mm) and in azimuthal direction(σ_ϕ in mm). From panel (a) one sees that the maximum drift time is less than 50 μs. In panel (b), the maximum accumulated deflection angle is shown to be less than 6 degrees. In panel (c), the maximum cluster width in pad direction is 1.2 mm, and 300 ns in time direction. The rise of σ_{tim} with increasing r is due to the dip angle of the track with respect to the pads. Panel (d) shows that the two-track resolutions at $r = 8$ cm (where the particle track density is highest) are 7 mm in radial direction, and 1 mm in azimuthal direction, respectively.

6.2 Tracking Performance

The key questions about the FTPC tracker are:

- In what rapidity range is tracking possible?
- What fraction of primaries in the acceptance range of the FTPCs is actually reconstructed?
- How many background tracks are accepted by tracking?

Inasmuch as the maximum number of hits a track can have is 10 (= number of pad rows in one FTPC), it is reasonable to require at least five hits per reconstructed track. Fewer give less accurate momentum measurement and charge determination and less efficient rejection of non-primaries. With this constraint, the η range of acceptance for high momentum particles is $2.6 \leq |\eta| \leq 4.0$; it is given by the dimensions of the FTPCs and the position of the pad rows.

The performance of the tracker in this region can be judged by two quantities: The first is the efficiency, i.e. the ratio of the number of primaries which are properly reconstructed compared to the number of primaries traversing the FTPCs in the valid η range. The second measure is the contamination, the fraction of the reconstructed tracks due to non-primaries. Contamination comes either from tracks reconstructed from hits from different original tracks, or from tracks from non-primary particles. Results of simulations, using HIJING events of central Au+Au collisions, GEANT simulations of multiple scattering and secondary interactions, as well as a simulation of diffusion and measuring errors, are given as function of η in Fig. 25 for different beam-pipe geometries.

As can be seen, the efficiency drops substantially, and the contamination rises, for $|\eta| \geq 3.5$. The reasons are the following:

- The spatial hit density is largest at small radius (large η).
- A larger value of η corresponds to a smaller angle between the beam axis and a track. Hence, the projected length *tlc* of the track, Fig. 23, is much smaller than for small η. These shorter track projections make twist less precise, so identification of non-primaries is less certain.
- For $|\eta| > 3.7$ the number of hits is less than ten. Therefore it is more difficult to identify non-primaries.

It is believed that additional fine tuning of the tracking parameters and/or algorithms can further improve the present performance.

As is evident form the top panel in Fig. 25, the simulations show that a beam pipe with a steel section starting at $z = \pm 76.2$ cm causes a striking increase of contamination due to a large number of hits from secondary production. For each hit of a primary, two hits from non-primaries are predicted; this is based on GSTAR/g2t simulations with central Au+Au events from the HIJING generator. However, replacement of this steel by aluminum reduces the contamination by about 60% and increases the efficiency significantly (see lower two panels of Fig. 25).

Another important consequence of the steel beampipe is that the effect of multiple scattering makes some of the tracks in the FTPC appear not to have originated from the IP. (incorrect relation between R, tlc and τ). When this discrepancy is outside the tolerance, this primary track would be classified as secondary or rejected.

6.3 Momentum and Charge Determination

The reconstructed momentum, p, and transverse momentum, p_T, are compared with the corresponding exact values in Fig. 26. This analysis is again based upon HIJING Au+Au central collision events. The cluster measuring accuracy was calculated according to the standard TPC formulae [blu93] using the appropriate diffusion coefficients (Fig. 12) and pad response width (0.6 mm). One concludes that the momentum resolution is about 12.5% and suffers less than the tracking efficiency and contamination from the steel in the standard beam pipe.

The accuracy of measurement for the invariant momentum differences ΔQ_{inv} for pairs of equal charge particles was found to be approximately 35 MeV/c. Concerning an HBT analysis, such a value of ΔQ_{inv} corresponds to a source radius of about 6 fm. Such values of the radius parameter have been found in Pb+Pb central collisions at the CERN SPS. Measurement via the FTPC will require a careful unfolding of the resolution and the sensitivity to substantially larger source sizes is clearly limited.

The charge determination efficiency, i.e. the percentage of charges correctly assigned by the track reconstruction, is at least 96 %, even using the standard beam pipe. This value improves further when a low-Z material is chosen for the beam pipe, or if only tracks with 10 hits are considered.

6.4 Two-Track Resolution

To evaluate the two-track resolution, we implemented in a slow simulator the same algorithms for transporting the electron clouds as was done for Fig. 24. Particles given by an event generator are processed by the Geant program (GSTAR). All the hits were propagated towards the readout position. Each particle track produced one hit per pad row. Finally, two-dimensional charge distributions were obtained as function of pad number and time bin for all the pad rows. Such information is useful not only for assessing two-track resolutions, but also for tuning the cluster finder, and for estimating the data volume for the DAQ system.

Fig. 27 gives the charge distribution for three close hits (radial separation 7 mm, azimuthal separation 1.5 mm) originating at $r = 8$ cm. This demonstrates the excellent intrinsic two-track resolution of the FTPC at this radius and confirms the results shown in Fig. 24d.

6.5 Detector Occupancy

A typical pixel-occupancy plot is shown in Fig. 28 for a Be beam-pipe configuration using one VENUS event. It is encouraging to see that most clusters are well separated. The mean occupancy is about 13%. However, for a beam pipe partially made from stainless steel, the occupancy almost doubles to 23%. More cluster merging occurs at smaller radii where the hit density is larger. The performance of the FTPCs would be adversely affected by such a beam-pipe configuration, as already discussed.

6.6 dE/dx Considerations

Because of only 10 dE/dx samplings, with 2 cm pad length, the FTPC's capability for particle identification is marginal. Nevertheless, we have simulated the dE/dx resolution. A gas mixture of Ar-CO_2(50%) is used. Fig. 29 shows the plots of the normalized truncated mean $\langle dE/dx \rangle$ as a function of momentum. This mean is an average of the lower 80% of samples. Most hadrons are in the relativistic-rise region.

The widths of the dE/dx distribution for both protons and pions are about 25% (FWHM). As anticipated, one can not resolve protons from pions. Nevertheless, the measurements of $\langle dE/dx \rangle$ may be useful. Two points can be made: (1) In the nuclear-stopping analysis, one can reduce the statistical error of the $N(+) - N(-)$ spectrum by applying a two-dimensional cut around protons in the distribution of $\langle dE/dx \rangle$ vs. momentum; (2) One may use the measured $\langle dE/dx \rangle$ to look for any charged particles with $|Z| > 1$, produced by coalescence or rare processes.

6.7 The Limitations of a One-Plane Detector

It had once been suggested to consider the possibility of using a single detector plane as a simpler way of determining the pseudorapidity of particles in the forward direction. In order to simulate this situation we have looked at hits produced by HIJING and GEANT for central Au+Au events in the first plane of the FTPC. All parts of the STAR detector were included in the simulation. Background from secondary particles is known to be a problem, particularly for a realistic design of the beam pipe. For the most optimistic estimate we used a 1-mm-wall Be beam pipe over the full length of the apparatus. The distribution of radial position of hits in the first plane is shown in Fig. 30 which shows all hits, primary particles, non-primaries, and gives the ratio of primaries to non-primaries. The pseudorapity covered by this single plane is $\eta = 2.4$ to 3.7.

There is clearly a very poor signal-to-background ratio as is evident from Fig. 30 (d). The question arises whether this could be corrected for. Since there is a large contribution from secondary particles produced by primaries in pseudorapidities beyond where STAR has good measurements, the pseudorapidity distributions would, at best, be extremely difficult to correct on an average basis, and virtually impossible on an event-by-event basis. It is concluded that such a one-plane detector would be badly lacking compared to the proposed FTPC.

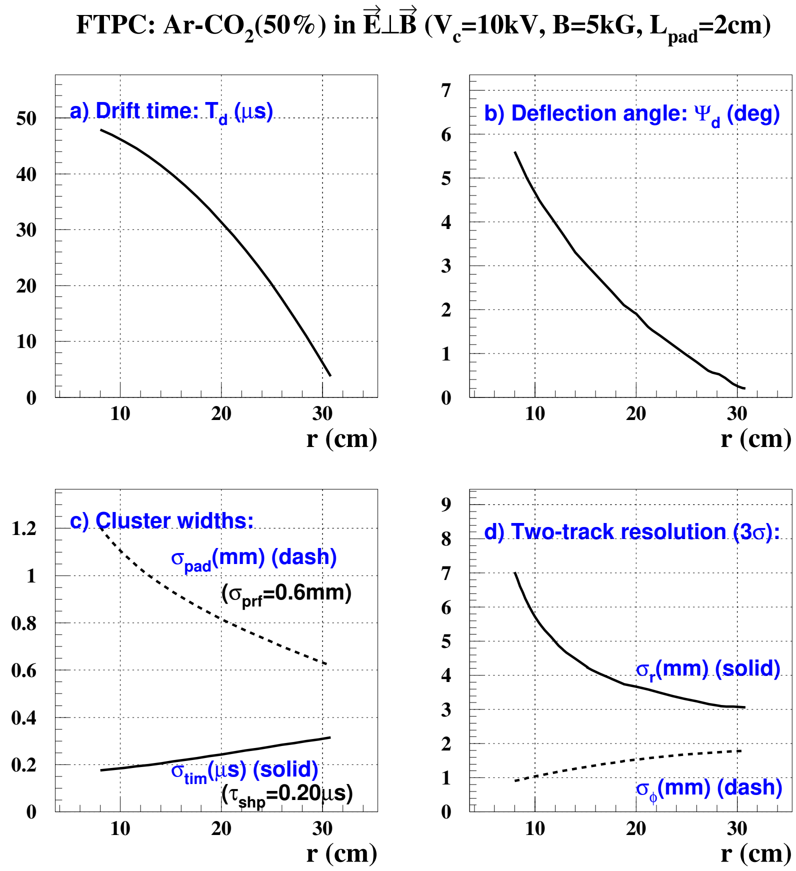

Figure 24: Electron-cluster properties as a function of the radial position of the hit for the FTPC design. (a) drift time; (b) deflection angle; (c) cluster widths in time direction (solid line in μsec) and in pad direction (dashed line in mm); (d) two-track resolution (3σ) in the radial direction (solid line) and in the azimuthal direction (dashed line).

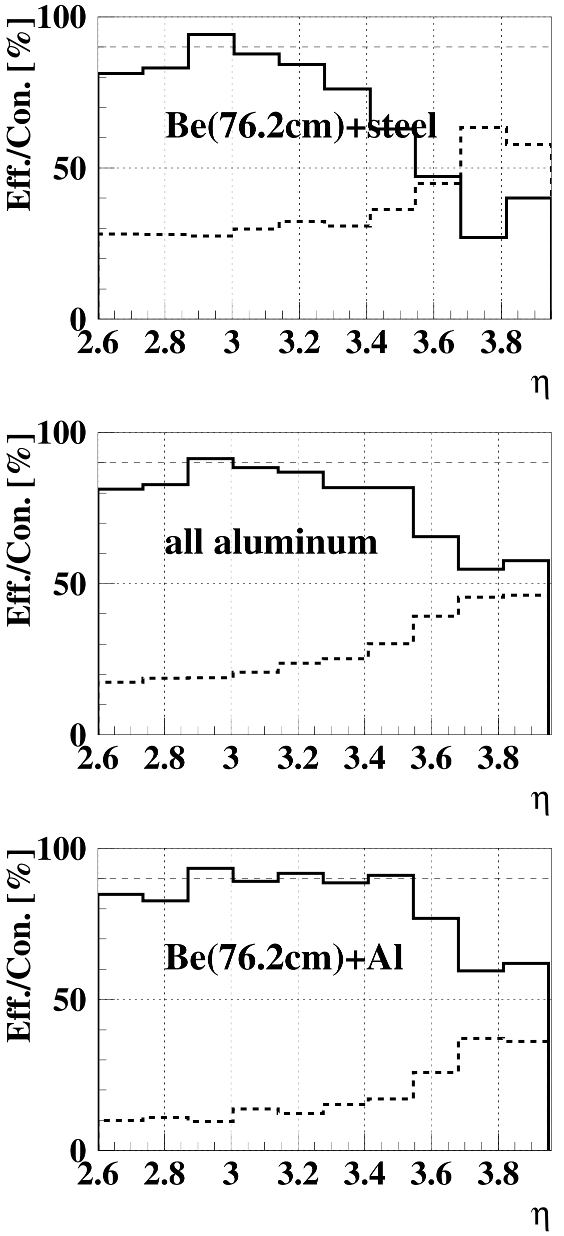

Figure 25: Efficiency (solid line) and contamination (dashed line) as function of η for different beam-pipe geometries.

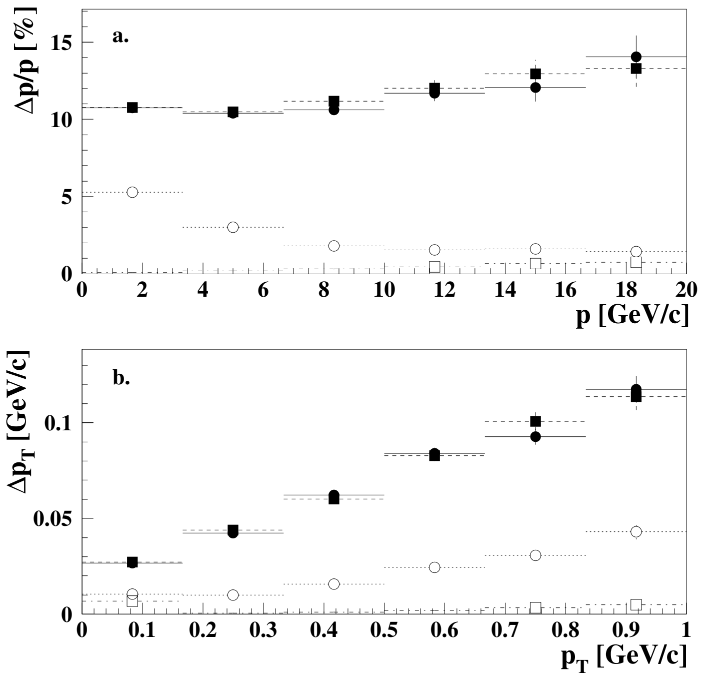

Figure 26: Resolution for (a) momentum p and (b) transverse momentum p_T. Multiple scattering off is open symbols: the open square is for tracks with 10 hits, and the open circle is for 5-9 hits. Multiple scattering on is filled symbols: the filled circle is for standard beam pipe, and the filled square is for all-beryllium beam pipe.

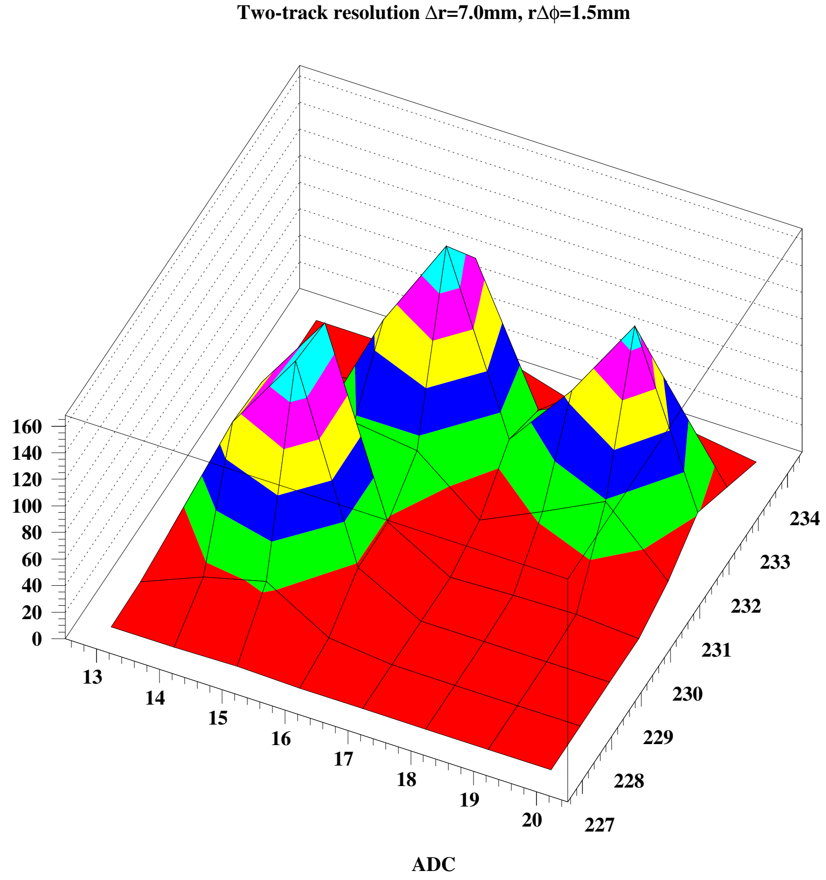

Figure 27: Two-track resolution according to the FTPC slow simulator.

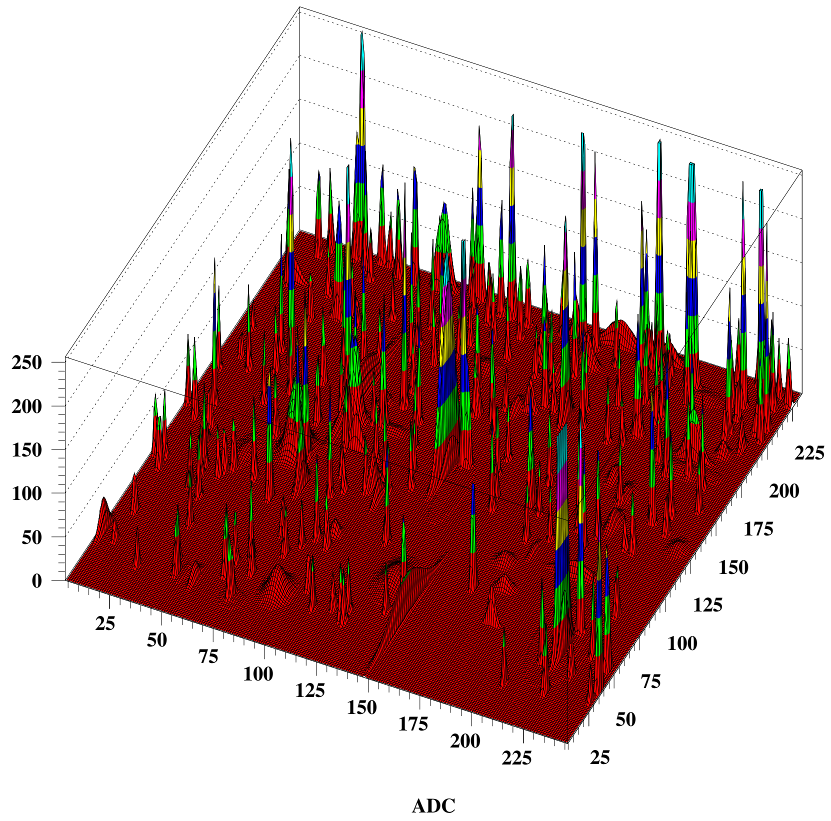

Figure 28: Pixel occupancy in a section of the FTPC chamber when using an all-Be beam pipe.

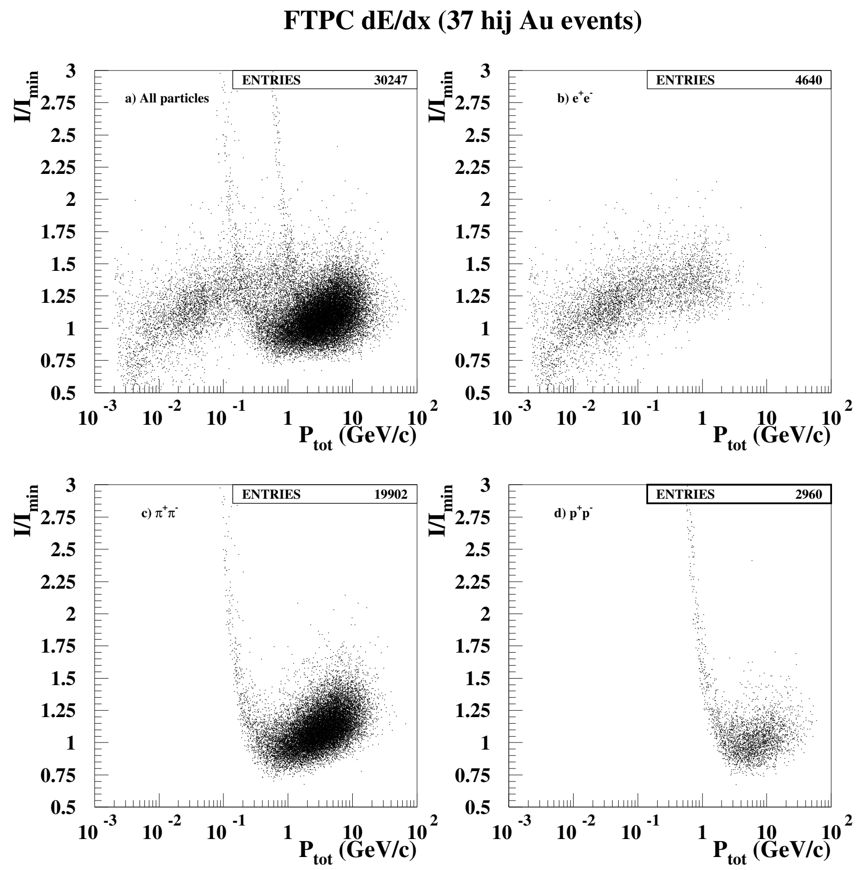

Figure 29: Normalized $\langle dE/dx \rangle$ measured in the FTPC as function of particle momentum. (a) for all charged particles; (b) for electrons and positrons; (c) for charged pions; (d) for protons and antiprotons.

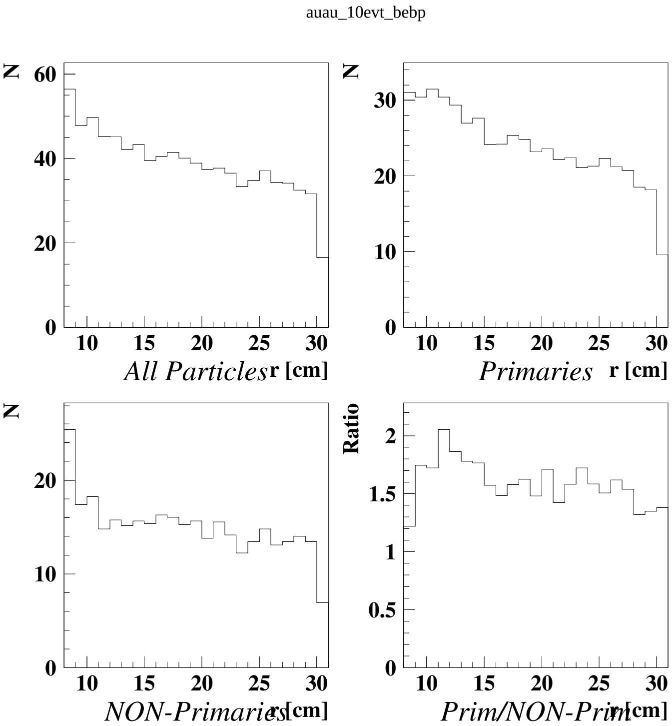

Figure 30: Hits in the first plane of the FTPC with an all-beryllium beam pipe for all particles (top left), primary particles (top right), and non-primary particles (bottom left). The panel at bottom right shows the ratio of primaries to non-primaries.

7 Laser Calibration System

7.1 Purpose

The laser calibration system for the FTPCs is needed for three primary purposes:

- It will serve as the absolute calibration of the effective drift velocity, which is essential for accurate track location along the radial direction. Recall that the $1/r$ electric field means radius-dependent drift velocity.
- It will provide calibrated, straight beams from which to infer corrections for spatial distortions.
- It will serve as a permanently available testing facility for the FTPCs.

7.2 Requirements

The requirements for a good measurement of drift velocity are more demanding in a radial drift TPC than in a standard configuration because the drift velocity is non-uniform. The electric field can be held to vary as $1/r$ relatively accurately; however, the drift velocity of a given gas is a non-linear function of electric field. Therefore, in order to accurately determine the spatial positions of the hit clusters, it is essential to measure the drift velocity as a function of r in the FTPCs. A single-point method, such as the use of the innermost hits of the tracks, is not adequate for determining a velocity profile, nor is a single external velocity monitor. An effective system must provide hits in calibrated locations at the various radii of the FTPC. The minimum configuration necessary to achieve these goals would have a total of five laser beams at various radii in a plane containing the detector axis. As shown in Fig. 31, three beams would be parallel to the axis of the detector, one at the innermost radius, one at the outermost radius, and one at an intermediate radius. Two additional beams would be tilted – one from inner radius at one end of an FTPC to outer radius at the other end of this FTPC, and vice versa for the other beam, to provide measurements at many radii. The straightness of the reconstructed diagonal tracks will test the correctness of the assumed dependence of drift velocity vs. radius.

To first order, the radial $\boldsymbol{E}$ is perpendicular to the axial $\boldsymbol{B}$ in the FTPCs, but there is a small radial component of $\boldsymbol{B}$ at the large-$|z|$ end of each FTPC. The small resulting effect on the drift will also be calibrated by the laser.

Finally, physical deformations of the FTPCs due to the mechanical mounting and gravity might result in small distortions. These spatial distortions will require sets of calibrated laser beams at several different azimuthal angles. We plan to have three planes of laser beams, each plane being displaced by 120 degrees in azimuth. Thus, there will be a total of fifteen beams, for each of the two FTPCs.

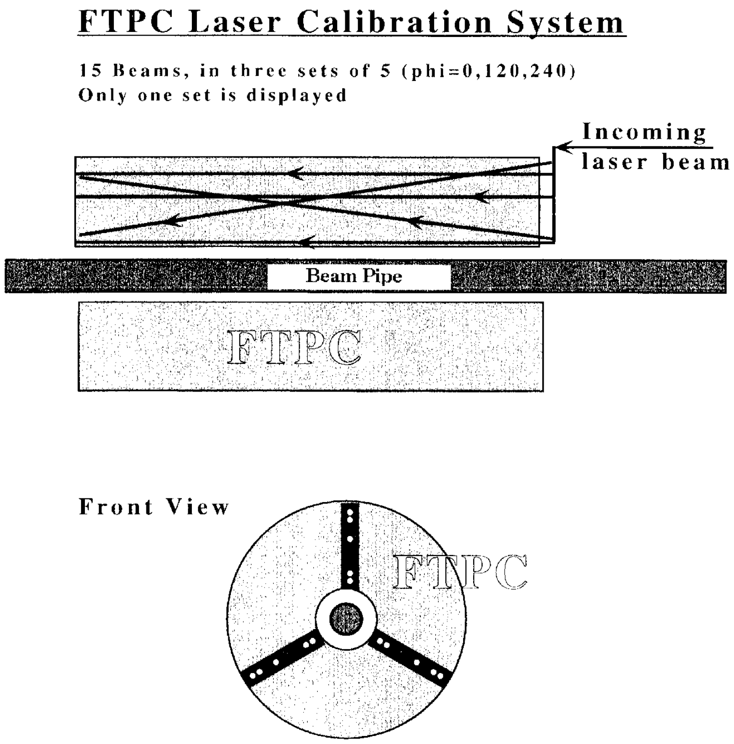

Figure 31: Schematic of laser calibration beams.

The uncertainty in the laser beam locations should be significantly smaller than the spatial precision in hit reconstruction of a few hundred μm. Pulse-to-pulse measurements of one of the laser beams, using either quadrant silicon detectors or two-dimensional Position Sensitive Detectors, would meet this level of accuracy for a single reference beam. An empirical map of the locations of all other laser beams relative to this single measured beam would be utilized to determine the pulse-to-pulse locations to the required accuracy.

The wavelength and power of the laser beams must be appropriate to ionize the FTPC gas at a level at least comparable to minimum ionizing tracks. The ionization properties of the "cool" gas in the FTPC are different from the customary P10 gas. Individual beams of 1 mm diameter and an energy of 10 μJ in energy from a Nd:YAG laser operating on the fourth harmonic would probably meet this requirement. At times, up to an order of magnitude more energy would be desirable for more accurately determining the pulse-to-pulse variation of the centroid of the charge distribution on the pads.

7.3 Description of Laser System

We propose to use a Nd:YAG laser, run on the fourth harmonic (266 nm), as the power source for the calibration system. We would either purchase a dedicated laser or borrow time from the laser used by the main TPC calibration system. A polarizer will be installed along the beam path to regulate laser power. A UV telescope system will be used to expand/reduce the primary beam to produce a 1-cm diameter beam of uniform energy profile. This beam will be transported through light-tight pipes from the laser house, which is external to the STAR magnet's iron return yoke, into the bore hole at $\eta = 2.0$ of the magnet pole tip. From the pole tip, the laser beam will take a straight path to a fused silica window in the gas containment wall of the FTPCs. Alignment of the incoming laser beam can be maintained with two 2-axes mirror mounts. These mirrors will be driven by piezo actuators (required by the magnetic field) which will be controlled through a computer interface. The computer will receive feedback on the accuracy of the laser alignment from silicon diodes at two locations along the beam path. One of these control mirrors will be mounted close to the Nd:YAG laser, ensuring that the beam is delivered accurately to the distribution system. The second will be at the entrance to the distribution system, ensuring that the calibration beams are accurately delivered to the FTPCs.

The distribution optics will be contained in the region between the gas containment wall and the field cage, and they will be supported on rails inside a thin wall tube. The rails will be made of either glass or ceramic, as they must be able to stand off the high voltages of the FTPC drift field, and must provide the rigidity necessary for the spatial resolution requirement. 2-cm diameter mirrors at the outer radius position which will direct the 1-cm beam along the rail toward the inner radius. This 1-cm beam will be intercepted along its path by five 1-mm diameter pick-off mirrors, at five radii, which produce the five calibration beams. The remainder of the 1-cm beam will be absorbed at the end of the tube.

Once the primary laser beam penetrates the gas-containing wall of the FTPC, each mirror is 100% reflecting. For the mirrors to produce the 1-mm beams, we are considering using 1-mm diameter glass rods cut at the appropriate angle and made totally reflecting at that cut surface by an inorganic dielectric coating. This is the method used in the main TPC.

To distribute the primary laser beam to the three sets of calibration beams we are considering two possible methods. One is to have a three-position 90-degree mirror which is mechanically rotated to any one of three azimuthal directions to supply the broad beam needed for any one set of five 1-mm mirrors. The motive power for rotation can be derived from the $\boldsymbol{B}$ field of the STAR solenoid plus a current coil, or by hand when the magnet is off. The other approach is to have a single three-angle mirror (three faces) which simultaneously supplies all three beams for 15 mirrors at once. This latter approach requires more beam energy from the laser, but has no moving parts.

8 Integration into STAR

8.1 Mechanical

The FTPC positions and dimensions are determined by the locations of the surrounding detectors (SVT, TPC amd VPD) and the magnetic field configuration. The present design allows the maximum possible acceptance, and minimizes interference with the other detectors.

The length in the z direction is limited by the particle density on the end nearest to the interaction point (IP), and by the increasing magnetic field inhomogeneity on the other end. The outer diameter is limited by the required safety distance to the Inner Field Cage (IFC) of the TPC and the needed space for the SVT support, cables and cooling. The inner diameter is determined by the size of the vacuum beam pipe. For exact dimensions see the envelope drawing (Fig. 32).

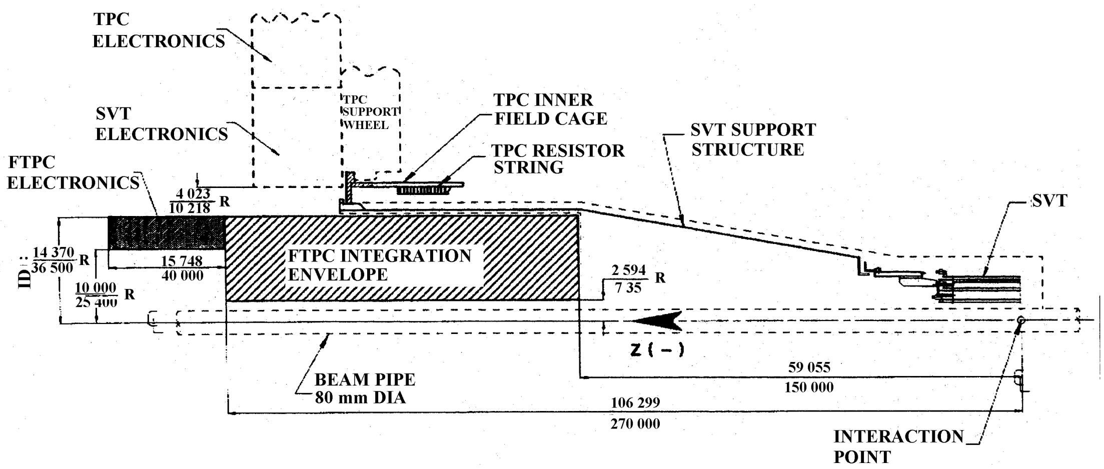

Figure 32: Envelope of FTPC.

The mechanical mounting is shown in Fig. 33. There are four fixation points at the "interface ring" between the IFC, SVT and FTPC. The FTPC load (approx. 350 lbs) is supported by the TPC wheel. There is no rigid connection with the SVT support.

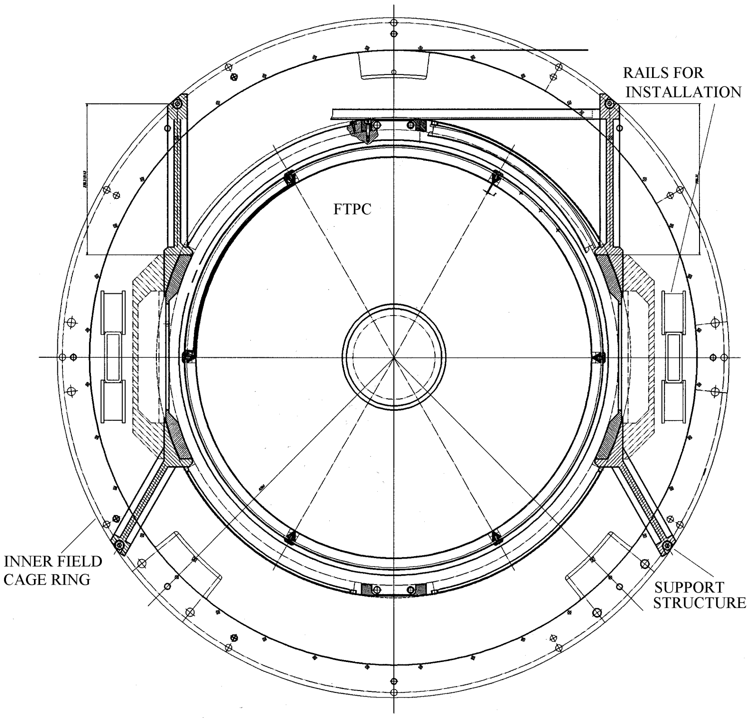

Figure 33: Mechanical Mounting of FTPC - end view.

8.2 Installation

The inner free FTPC diameter is 14.7 cm such that the whole detector can be moved outwards along the beam pipe towards the wall of the experimental hall, where the vacuum pipe diameter is 12.7 cm. The cylindrical FTPC structure requires an open vacuum beam pipe for the first installation.

For movements along the beam axis and the adjustment in the final position, a rail system common with the SVT is used, which will be removed for the running periods. The same system allows easy rolling out of the eastward FTPC in the case of necessary access to the SVT detector. For this procedure, only the 12 readout boards have to be uncabled.

During the vacuum bakeout the FTPC can stay in position or in another region where the beam pipe is 8 cm in diameter. There the distance between beam pipe and FTPC is large enough to accomodate a heat blanket and an air- or water-cooled heat shield to protect the detectors. A Be-Al beam pipe would be advantageous also for bakeout, because of the lower bakeout temperature for that material in comparison to stainless steel.

8.3 Cooling

The total power consumption of electronics for one FTPC is less than 400 W. This heat production is homogenously distributed over 2 m^2 and could be cooled by air. But this would require airducts with diameters in the order of 10 cm. Water cooling is much more efficient and space saving and therefore is likely to be used. Corrugated cooling sheets of 0.2 mm thickness are mounted close to the FEE boards. Each sheet covers 5 FEE boards and is cooled by 4 copper tubes of 3 mm diameter and 0.3 mm wall thickness. The interconnection is made with short silicone tubes. The system operates at slight underpressure avoiding the outflow of water into the electronics in the case of leaking. These cooling sheets cover approx. 70% of the cylindrical surface and represent between 0.5% and 1.5% of a radiation length depending on the choice of material. To avoid interferences with the cooling systems of the IFC resistor chain and of the SVT electronics, the FTPC will have a thin shield at the outermost diameter which encloses the compartment with its FE electronics.

8.4 Data Acquisition

The complete readout electronics chain is nearly identical with the main TPC; see also section 4.2. The total amount of TPC data is increased by 20% for the standard beam pipe with stainless steel, or about 10% when using a Be-Al beam pipe. This additional data load does not exceed any critical limits in the data acquisition system, events are just written a little more slowly.

8.5 Rack Space and Cables

Three racks (I-B5-7) on the first floor of the south platform are expected to house the low- and high-voltage power supplies, gating pulser and, eventually, laser equipment. Two racks are foreseen in the control room (DAQ A 14-15) for the readout crates and third level trigger. Cables are already included in the STAR integration plan. They will run parallel to the main TPC cables up to the TPC wheels, and from there to the FTPC.

8.6 Slow Control

The main operation parameters like voltages, temperatures and pressure must be monitored very carefully during running time, and should be included in the common STAR Slow Control System.

9 Responsibilities, Cost Estimate and Schedule

9.1 Responsibilities

The complete detector configuration to accomplish the physics goals includes the following subsystems:

- Two FTPCs, one on each side, consisting of the gas vessel, the field cage and the readout chambers
- Readout electronics up to the storage computer
- Gas supply system and cooling
- Laser System
- Auxiliary equipment, like gate and calibration pulsers and monitoring hardware.

The participating groups share the work for the subsystem as follows:

BNL is responsible for the DAQ part of the readout electronics and will contribute to the infrastructure and to the gas system.

LBNL provides the ASIC chips for the FEE boards and the readout boards.

MPI is designing and constructing both FTPCs (gas vessel, field cage and readout chambers). It manufactures the FEE boards and contributes to the systems for gas, laser beams and monitoring.

MEPHI contributes to the design and components of the laser system.

UC Davis is taking responsibility for the design and the procurement of the laser system.

UCLA is loading the electronic boards for the gate and calibration pulsers.

STAR/RHIC is expected to provide parts of the general infrastructure, like electricity, cable trays, water etc.

9.2 Cost estimate

The cost estimate is based on an engineering study for the field cages and on the well known production costs for the readout chambers.

The largest capital expenditure items of the project, i.e. electronics and DAQ, are very precisely defined, inasmuch as identical equipment is used for the main TPC, already under construction.

The costs estimated for the smaller items are based on experience and/or on the knowledge of costs for some of the needed components. A summary of the estimated capital costs in 1997 $ is shown in Table 4.

Table 4: **FTPC Costs and Institutional Contributions (all k$).**

	Total Cost	BNL	LBNL	MPI	MEPHI	UC Davis	UCLA	STAR/ RHIC
Field Cages	75			75				
Readout Chambers	150			150				
Frontend Electr.	290		145	145				
Gas System	60	30		30				
Laser System	90			50	(x)	40		
HV + LV Supply	35			35				
Calibr. + Gate Pulser, Monitor	25			25			(x)	
Cooling System	25		10	15				
DAQ + Computing	220	180		40				
Infrastructure	80	20		20				40
Contingeny (10%)	100	25	15	60				
Sum of column	1150	255	170	645		40		40

In addition to the above investment money, the institutions provide the necessary manpower for the design, installation and construction of the various parts of the FTPC system and support for travel. The largest amount of technical support will be provided by MPI: 2.5 manyears of engineers (mechanics and electronics), 12 manyears of technicians and 4.5 manyears of programmers are foreseen. This support amounts to a contribution of about 2 M$ (without overhead costs) in addition to the investment money.

9.3 Schedule

The schedule estimate is shown in Fig. 34. For this profile it is assumed that the required manpower and funding are available as planned. Under these assumptions, the complete detector could be delivered to BNL in summer 1999 and installed during the first long shutdown. But in any case, the completion would be possible for the shutdown during 2000.

Table 6.2: FTPC Construction Schedule

Nr.	Component/task	Days	Start	End
1	STAR -FTPC	519	01.08.97	28.07.99
2	Electronic FEE Boards	366	01.08.97	25.12.98
10	Readout- and DAQ-Boards	130	01.10.98	31.03.99
12	Monitor Electronics	100	02.01.98	21.05.98
14	Chamber Body	421	15.08.97	26.03.99
19	Field Cage	126	15.08.97	06.02.98
23	Readout Chambers	431	15.10.97	09.06.99
30	Electronic Cooling	100	01.05.98	17.09.98
33	Laser System	163	17.08.98	31.03.99
35	Auxiliary Equipment	60	01.04.98	23.06.98
41	Test Equipment	101	01.05.98	18.09.98
45	Assembly (MPI)	60	01.04.99	23.06.99
51	Transport Equipment	30	01.10.98	11.11.98
54	Transport (to BNL)	20	01.07.99	28.07.99

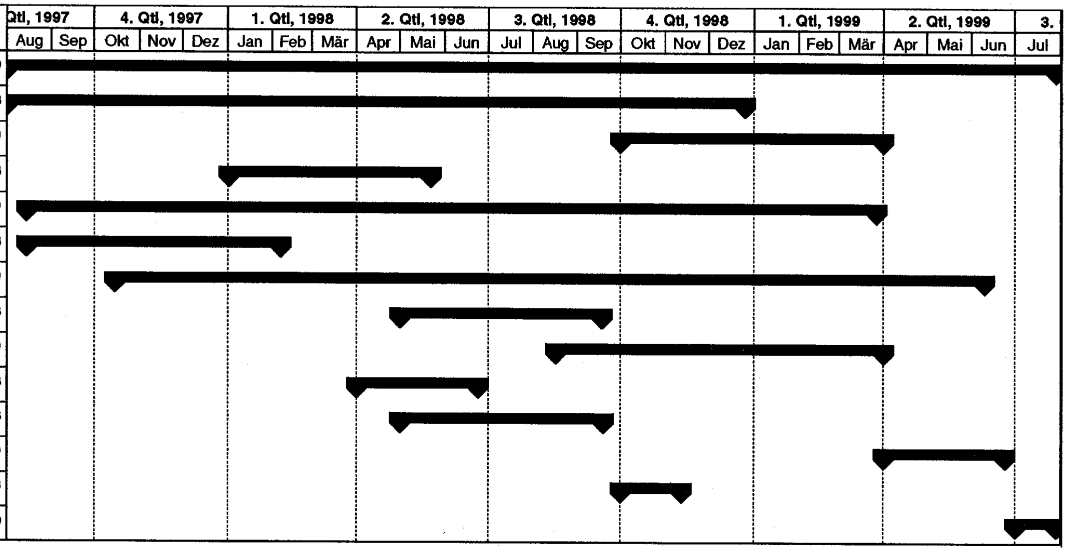

Figure 34: FTPC Construction Schedule.

References

[bet96] W. Betts, et al., Results from the STAR TPC System Test. preprint CU (Creighton U.) -PHY-NP 96/03, Nov. 1996, submitted to IEEE Transactions on Nuclear Science;
S. Klein, et al., Front-End Electronics for the STAR TPC, IEEE Transactions on Nuclear Science **43**, 1768 (1996).

[bia89] S. Biagi, MAGBOLTZ program, Nucl. Instr. Meth. **A283** (1989) 716

[bit97] X. Bittl, V. Eckardt, H. Fessler, W.G. Gong, M. Konrad, A. Mock, A. Odian, P. Seyboth, J. Draper, M. Hildebrandt, K. Ness, B. Schmidt. *Diffusion and Drift Studies of Ar-DME/CO_2/CH_4 Gas Mixtures for a Radial TPC in an $E \perp B$ Field.* Nucl. Inst. Meth. **A398** (1997) 249; STAR Note 284.

[blu93] W. Blum and R. Rolandi: Particle Detection with Drift Chambers, Springer-Verlag, Berlin, 1993

[boi97] B. Boimska et al., Update on discharge studies in MSGCs, CMS-Tracking Note, TN/97-20.

[dra95] J. Draper, *External TPC Performance and Simulations*, pages 23-32 of STAR Note 211 (1995). See also contributions to Plenary Sessions of STAR Collaboration meetings, 1995-96, for improvements on these algorithms.

[gei97] K. Geiger and R. Longacre; preprint nucl-th/9705041, May 1997

[gei95] K. Geiger, Phys. Rep. **258** (1995) 237

[kle97] S. Klein and E. Scannapieco, LBL-40457, June, 1997, to appear in the Proceedings of *Photon '97.*

[kle95] S. Klein and E. Scannapieco, STAR Note 243, Feb. 1995, available at http://www.rsgi01.rhic.bnl.gov/star /starlib/doc/www sno/ice/sn0243.html.

[kon97] M. Konrad, PhD thesis, TU Munich, 1997, MPI-PhE/97-15.

[lon] R. Longacre, private communication

[mil95] Z. Milosevich, 2/95 web page of trigger group on STAR homepage.

[nes93] K. Ness, *Spherical-harmonics Decomposition of the Boltzmann Equation for Charged-particle Swarms in the Presence of Both Electric and Magnetic Fields.* Phys. Rev. **E47** (1993) 327
K. Ness, Aust. J. Phys. **48** (1995) 557
J. Draper and K. Ness, *Quantitative Electron Diffusion/Drift via Moments Method and Magboltz*, to be submitted to Nucl. Instr. Meth.

[nys97] J. Nystrand, S. Klein, E. Scannapieco, to appear in the Proceedings of *Hadron '97*.

[pra93] S. Pratt, Phys. Lett. **B301** (1993) 159

[raj93] K. Rajagopal and F. Wilczek, Nucl. Phys. **B399** (1993) 395; **B404** (1993) 577
S. Gavin, Nucl. Phys. **A590** (1995) 163c

[whi96] J. Whitfield, Thirteenth STAR Collaboration Meeting Plenary Minutes, 8/96, page 558.

[wan91] X.-N. Wang, M. Gyulassy, Phys. Rev. **D44** (1991) 3501